The Astrophysical Journal, 964:18 (23pp), 2024 March 20 https://doi.org/10.3847/1538-4357/ad23ed

Resolved Measurements of the CO-to-H_2 Conversion Factor in 37 Nearby Galaxies

I-Da Chiang (江宜達)[1], Karin M. Sandstrom[2], Jérémy Chastenet[3], Alberto D. Bolatto[4], Eric W. Koch[5], Adam K. Leroy[6,7], Jiayi Sun (孙嘉懿)[8,9,10], Yu-Hsuan Teng[11], and Thomas G. Williams[12,13]

[1] Institute of Astronomy and Astrophysics, Academia Sinica, No. 1, Sec. 4, Roosevelt Road, Taipei 10617, Taiwan; idchiang@asiaa.sinica.edu.tw
[2] Department of Astronomy & Astrophysics, University of California, San Diego, 9500 Gilman Drive, La Jolla, CA 92093, USA
[3] Sterrenkundig Observatorium, Universiteit Gent, Krijgslaan 281 S9, B-9000 Gent, Belgium
[4] Department of Astronomy, University of Maryland, College Park, MD 20742, USA
[5] Center for Astrophysics| Harvard & Smithsonian, 60 Garden Street, Cambridge, MA 02138, USA
[6] Department of Astronomy, The Ohio State University, 4055 McPherson Laboratory, 140 West 18th Avenue, Columbus, OH 43210, USA
[7] Center for Cosmology and Astroparticle Physics, 191 West Woodruff Avenue, Columbus, OH 43210, USA
[8] Department of Physics and Astronomy, McMaster University, 1280 Main Street West, Hamilton, ON L8S 4M1, Canada
[9] Canadian Institute for Theoretical Astrophysics (CITA), University of Toronto, 60 St George Street, Toronto, ON M5S 3H8, Canada
[10] Department of Astrophysical Sciences, Princeton University, 4 Ivy Lane, Princeton, NJ 08544, USA
[11] Center for Astrophysics and Space Sciences, Department of Physics, University of California, San Diego, 9500 Gilman Drive, La Jolla, CA 92093, USA
[12] Max-Planck-Institut für Astronomie, Königstuhl 17, D-69117 Heidelberg, Germany
[13] Subdepartment of Astrophysics, Department of Physics, University of Oxford, Keble Road, Oxford OX1 3RH, UK
Received 2023 October 28; revised 2024 January 24; accepted 2024 January 30; published 2024 March 12

Abstract

We measure the CO-to-H_2 conversion factor (α_{CO}) in 37 galaxies at 2 kpc resolution, using the dust surface density inferred from far-infrared emission as a tracer of the gas surface density and assuming a constant dust-to-metal ratio. In total, we have ∼790 and ∼610 independent measurements of α_{CO} for CO (2–1) and (1–0), respectively. The mean values for $\alpha_{CO\,(2-1)}$ and $\alpha_{CO\,(1-0)}$ are $9.3^{+4.6}_{-5.4}$ and $4.2^{+1.9}_{-2.0}$ $M_\odot$ pc^{-2} (K km s^{-1})$^{-1}$, respectively. The CO-intensity-weighted mean is 5.69 for $\alpha_{CO\,(2-1)}$ and 3.33 for $\alpha_{CO\,(1-0)}$. We examine how α_{CO} scales with several physical quantities, e.g., the star formation rate (SFR), stellar mass, and dust-mass-weighted average interstellar radiation field strength ($\overline{U}$). Among them, $\overline{U}$, Σ_{SFR}, and the integrated CO intensity (W_{CO}) have the strongest anticorrelation with spatially resolved α_{CO}. We provide linear regression results to α_{CO} for all quantities tested. At galaxy-integrated scales, we observe significant correlations between α_{CO} and W_{CO}, metallicity, $\overline{U}$, and Σ_{SFR}. We also find that α_{CO} in each galaxy decreases with the stellar mass surface density ($\Sigma_\star$) in high-surface-density regions ($\Sigma_\star \geqslant 100\,M_\odot\,\mathrm{pc}^{-2}$), following the power-law relations $\alpha_{CO\,(2-1)} \propto \Sigma_\star^{-0.5}$ and $\alpha_{CO\,(1-0)} \propto \Sigma_\star^{-0.2}$. The power-law index is insensitive to the assumed dust-to-metal ratio. We interpret the decrease in α_{CO} with increasing $\Sigma_\star$ as a result of higher velocity dispersion compared to isolated, self-gravitating clouds due to the additional gravitational force from stellar sources, which leads to the reduction in α_{CO}. The decrease in α_{CO} at high $\Sigma_\star$ is important for accurately assessing molecular gas content and star formation efficiency in the centers of galaxies, which bridge "Milky Way–like" to "starburst-like" conversion factors.

Unified Astronomy Thesaurus concepts: Interstellar dust (836); Interstellar medium (847); Interstellar molecules (849); Far infrared astronomy (529); Dust continuum emission (412); Interstellar line emission (844); CO line emission (262); H I line emission (690)

1. Introduction

Star formation is fueled by the molecular gas in the interstellar medium (ISM). Thus, observing the molecular ISM is essential for studies of star formation and galaxy evolution. Unfortunately, the most abundant molecule in the ISM, H_2, is not directly observable in many cases in the cold molecular ISM due to its high transition energies ($h\nu/k_B \sim 510$ K) for the lowest rotational levels. As a result, low-*J* CO emission lines are the most widely used tracer for the molecular ISM, as the second most abundant molecule with strong millimeter rotational lines that can be excited at typical temperatures in molecular clouds. The standard practice is to use a CO-to-H_2 conversion factor α_{CO}, as follows

$$\Sigma_{mol} = \begin{cases} \alpha_{CO\,(1-0)} W_{CO\,(1-0)}, & \text{for CO (1–0)} \\ \alpha_{CO\,(2-1)} W_{CO\,(2-1)}, & \text{for CO (2–1)} \end{cases} \quad (1)$$

where Σ_{mol} [$M_\odot$ pc^{-2}] is the surface density of molecular ISM (including the mass of helium), α_{CO} [$M_\odot$ pc^{-2}(K km s^{-1})$^{-1}$] is the CO-to-H_2 conversion factor, and W_{CO} [K km s^{-1}] is the integrated intensity of the CO emission at the rest-frame frequency. The conventional α_{CO} in the Milky Way (MW) is α_{CO}^{MW} = 4.35 $M_\odot$ pc^{-2}(K km s^{-1})$^{-1}$ for CO (1–0).[14] In mass surface density units with a factor of 1.36 with helium included, this is equivalent to $\alpha_{CO\,(1-0)} = 4.35\,M_\odot$ pc^{-2}(K km s^{-1})$^{-1}$ (Solomon et al. 1987; Strong & Mattox 1996; Abdo et al. 2010). The "(1–0)" and "(2–1)" symbols represent the CO rotational transition from which α_{CO} is derived and W_{CO} is measured, i.e., CO (1–0) stands for the CO $J = 1 \rightarrow 0$ rotational transition at ∼115 GHz ($\lambda \sim 2.6$ mm) and CO (2–1) stands for the CO $J = 2 \rightarrow 1$ rotational transition at ∼230 GHz ($\lambda \sim 1.3$ mm). In this work, we focus on the $^{12}C^{16}O$ isotopologue and use CO for $^{12}C^{16}O$ for simplicity.

[14] In column density units, the standard MW conversion factor is $X_{CO\,(1-0)} = 2 \times 10^{20}$ cm^{-2}(K km s^{-1})$^{-1}$, where only H_2 is considered.

CO (1–0) had been the most frequently measured CO transition, and $\alpha_{CO\,(1-0)}$ is thus the fiducial case for α_{CO} in the literature. Meanwhile, CO emission from the next highest rotational level, i.e., CO (2–1), has become more and more common with modern instruments, e.g., ALMA, throughout the last decade. Directly deriving $\alpha_{CO\,(2-1)}$ has attained its own importance. Thus we will present both $\alpha_{CO\,(1-0)}$ and $\alpha_{CO\,(2-1)}$ in this work.

With the precise measurements of CO emission from modern instruments, our understanding of α_{CO} has become the factor that limits our ability to precisely study the molecular ISM and star formation in nearby galaxies. Observations have shown at least two main trends in the variation in α_{CO}. The first one is that α_{CO} tends to increase at lower metallicity or lower dust-to-gas ratios (e.g., up to ∼1 dex higher than the MW value at ∼0.2 solar metallicity; Israel 1997b; Leroy et al. 2011). This enhanced α_{CO} is often explained by the decrease in CO emission relative to the cloud mass defined by H_2 as shielding for CO weakened at lower metallicity (Papadopoulos et al. 2002; Grenier et al. 2005; Wolfire et al. 2010; Planck Collaboration et al. 2011; Genzel et al. 2012; Accurso et al. 2017; Gong et al. 2020; Madden et al. 2020; Hirashita 2023). This phenomenon is often known as the "CO-dark gas."

The second trend is that α_{CO} appears to be lower in the central ∼kpc of some galaxies (it can be a factor 5–10 times lower; Israel 2009a, 2009b, 2020; Sandstrom et al. 2013; Teng et al. 2022, 2023). It is also observed to be lower in (ultra) luminous infrared galaxies ((U)LIRGs; Downes et al. 1993; Downes & Solomon 1998; Papadopoulos et al. 2012; Herrero-Illana et al. 2019). This trend toward lower α_{CO} in galaxy centers and starbursts likely results from a combination of higher gas temperature, larger line width, and lower CO optical depth, which breaks the relationship between molecular cloud mass and line width that one would expect from isolated, virialized clouds (Shetty et al. 2011; Bolatto et al. 2013). This phenomenon is often referred to as the "starburst conversion factor." Because galaxy centers and (U)LIRGs tend to be bright in CO and thus easily observed, understanding this starburst conversion factor is important to make better use of a wide range of extragalactic observations in characterizing the star formation efficiency, gas dynamics, and H I-to-H_2 transition conditions.

Bolatto et al. (2013) proposed a formula for conversion factor treating the CO-dark gas and the starburst trend independently and simultaneously. This formula aimed to predict both the spatially resolved measurements from Sandstrom et al. (2013; including galaxy centers) and the (U) LIRGs measurements in Downes & Solomon (1998). The formula reads:

$$\frac{\alpha_{CO\,(1-0)}}{1\ M_\odot\ \mathrm{pc}^{-2}(\mathrm{K\ km\ s^{-1}})^{-1}} = 2.9 \times \exp\left(\frac{0.4}{Z'}\right) \times \begin{cases} (\Sigma^{100}_{\rm Total})^{-0.5}, & \Sigma^{100}_{\rm Total} \geqslant 1 \\ 1, & \Sigma^{100}_{\rm Total} < 1 \end{cases}. \quad (2)$$

Here Z' is the metallicity relative to the solar value, which traces the CO-dark gas effect; $\Sigma^{100}_{\rm Total}$ is the total surface density ($\Sigma_{\rm Total} = \Sigma_{\rm gas} + \Sigma_\star$) in units of $100\,M_\odot\,\mathrm{pc}^{-2}$, which is the proposed observational tracer and threshold for regions where a decrease in α_{CO} occurs, i.e., galaxy centers and (U)LIRGs. The authors found that with a threshold of $\Sigma^{100}_{\rm Total} \geqslant 1$ (a threshold related to self-gravitating giant molecular clouds), the relation $\alpha_{CO} \propto (\Sigma^{100}_{\rm Total})^{-0.5}$ reproduces the trend found in galaxy centers and ULIRG samples. A similar formula was also suggested by Ostriker & Shetty (2011), where the authors suggested a power-law relationship between α_{CO} and $\Sigma_{\rm gas}$ to describe the decrease in α_{CO} needed for their simulations to match observations. They showed that a relation of $\alpha_{CO} \propto \Sigma_{\rm gas}^{-0.5}$ over the surface density range 10^2–$10^3\,M_\odot\mathrm{pc}^{-2}$ brings the observations and simulations into agreement.

To better characterize how α_{CO} depends on local environments, spatially resolved measurements of α_{CO} are required. To measure α_{CO}, one needs to measure $\Sigma_{\rm mol}$ independently of the (single-line) CO intensity, and then divide it by the measured CO intensity. This could be achieved by several methodologies, e.g., using virial mass estimates (see the review in McKee & Ostriker 2007), modeling multiple spectral lines (e.g., Cormier et al. 2018; Teng et al. 2022, 2023), converting γ-ray emission (e.g., Abdo et al. 2010; Ackermann et al. 2012), and tracing the gas mass with the dust mass (Israel 1997a, 1997b; Leroy et al. 2007, 2009a, 2011; Bolatto et al. 2011; Planck Collaboration et al. 2011; Sandstrom et al. 2013; Schruba et al. 2017; den Brok et al. 2023). Based on existing resources, most of the methods are not practical for a survey in tens of nearby galaxies due to the requirement in target brightness or total observing time. The most feasible methodology is to use dust as a tracer for gas mass, where dust mass can be derived from infrared (IR) data observed with Herschel (Pilbratt et al. 2010), the Wide-field Infrared Survey Explorer (WISE; Wright et al. 2010), and Spitzer.

In this work, we measure α_{CO} with dust as the tracer for the total gas mass. We use dust masses derived from modeling the far-IR spectral energy distribution (SED) to trace the total gas mass. The key assumption we make is a constant fraction of heavy elements locked in the solid phase, i.e., a dust-to-metal ratio (D/M), which allows us to convert measurements of the dust surface density, H I surface density, and metallicity into molecular gas mass. The assumption of approximately constant D/M is supported by dust evolution models (Dwek 1998; Hirashita & Kuo 2011; Asano et al. 2013; Feldmann 2015) and kpc-scale measurements (Issa et al. 1990; Leroy et al. 2011; Draine et al. 2014; Vílchez et al. 2019; Chiang et al. 2021) in high-metallicity ($12 + \log(\mathrm{O/H}) \gtrsim 8.2$) galaxy disks, matching the region of interest in this work. In simulations (e.g., Aoyama et al. 2020; Choban et al. 2022), an approximately constant D/M results from efficient dust growth in the ISM, i.e., the majority of the refractory elements are locked in solid grains quickly. Although there are also studies that found variations in D/M with both depletion measurements (Jenkins 2009; Jenkins & Wallerstein 2017; Roman-Duval et al. 2019) and emission measurements (Roman-Duval et al. 2014, 2017; Chiang et al. 2018; De Vis et al. 2019), no widely agreed-upon prescription for the environmental dependence of D/M has been found thus far. The other reason we assume a constant D/M is that we anticipate the variation in D/M ($\leqslant$2 times) to be smaller in comparison to that of α_{CO} (up to ∼10 times) in normal galaxy disks.

Given the challenges in measuring spatially resolved α_{CO}, there have been few studies with large samples of resolved measurements in galaxies. Sandstrom et al. (2013) looked at the overlap of IR from KINGFISH (Kennicutt et al. 2011), CO from HERA CO Line Extragalactic Survey (HERACLES; Leroy et al. 2009b), and H I from THINGS (Walter et al. 2008) and made measurements of α_{CO} in 26 galaxies with ∼40″ resolution elements, which is the resolved study with one of the largest sample sizes. Most other studies in the field, e.g., Hunt et al. (2015), Accurso et al. (2017), and CO Multi-line Imaging of Nearby Galaxies (COMING; Yasuda et al. 2023), focused on galaxy-scale α_{CO}. Moreover, a survey of α_{CO} at a fixed physical scale, which allows us to evaluate the environmental dependence of α_{CO} fairly, is also missing as previous spatially resolved studies (e.g., Leroy et al. 2011; Schruba et al. 2012; Sandstrom et al. 2013) tend to perform their analysis at fixed angular resolution. In this work, we will measure α_{CO} across 37 nearby galaxies at a fixed ~2 kpc resolution. This study is made possible by several surveys of resolved CO intensities in the past two decades: the Nobeyama CO Atlas of nearby galaxies (CO Atlas; Kuno et al. 2007), HERACLES (Leroy et al. 2009b), the COMING project (Sorai et al. 2019), the Physics at High Angular resolution in Nearby Galaxies (PHANGS) Atacama Large Millimeter/submillimeter Array (ALMA) project (Leroy et al. 2021), and recent IRAM 30 m observations (PI: A. Schruba; see Leroy et al. 2022).

This paper is presented as follows. In Section 2, we explain our methodology for deriving α_{CO} from the data. We describe the data sets necessary for this work and how we constrain other physical quantities from observations in Section 3. We present the α_{CO} measurements and their correlations with local and galaxy-integrated conditions in Section 4. In Section 5, we investigate an observed power-law relation between α_{CO} and $\Sigma_\star$ in high-surface-density regions and provide a prescription for α_{CO} based on our findings. We discuss the physical interpretations of our results and how they compare to the literature findings in Section 6. Finally, we summarize our findings in Section 7.

2. Calculating α_{CO}

To calculate α_{CO}, we first estimate Σ_{mol} without using CO emission and an adopted conversion factor. In this study, we use a dust-based strategy to estimate Σ_{mol} by assuming a value for the fraction of metals locked in the solid phase, i.e., the D/M. The D/M is defined as:

$$\mathrm{D/M} = \frac{\Sigma_{dust}}{Z \times \Sigma_{gas}}, \tag{3}$$

where $\Sigma_{gas} = \Sigma_{atom} + \Sigma_{mol}$ is the total neutral gas surface density, Σ_{mol} is the molecular gas surface density, and the metallicity Z converts Σ_{gas} to a "metal mass surface density." By replacing Σ_{mol} in the above equation with the definition of α_{CO} in Equation (1), we have:

$$\alpha_{CO} = \Sigma_{mol}\, W_{CO}^{-1} = \left(\frac{\Sigma_{dust}}{Z \times (\mathrm{D/M})} - \Sigma_{atom}\right) W_{CO}^{-1}, \tag{4}$$

where Σ_{dust}, Z, Σ_{atom}, and W_{CO} are measurable quantities. Thus, by assigning a value of D/M, we can then calculate α_{CO} with our data set. The uncertainty in α_{CO} is propagated from the uncertainties in Σ_{dust}, metallicity, Σ_{atom}, and W_{CO}. The typical uncertainty in the pixel-by-pixel α_{CO} measurements in this work is in the range of 0.2–0.5 dex.[15]

Dust-based α_{CO} measurements in the literature usually have formulae similar to Equation (3) but with different assumptions. For example, Israel (1997b) and Leroy et al. (2009a) assumed a fixed dust-to-gas ratio (D/G) in their sample galaxies to derive α_{CO}. On the other hand, Sandstrom et al. (2013; see also Leroy et al. 2011; den Brok et al. 2023; Yasuda et al. 2023) assumed that the D/G remains approximately constant in a certain spatial region, e.g., kpc scale or entire galaxy. With this assumption, the authors are able to derive α_{CO} by minimizing the scatter in D/G in a group of nearby pixels, treating α_{CO} and D/G as free parameters. This method has the advantage of not forcing the value of D/G and the disadvantage of sacrificing the spatial resolution.

Generally speaking, we could assume different D/M values in each pixel when we apply Equation (4). However, despite the previous efforts to study the evolution of D/M (De Vis et al. 2019; Aoyama et al. 2020; Péroux & Howk 2020; Chiang et al. 2021; Choban et al. 2022; Roman-Duval et al. 2022), we do not have a well-established prescription of how D/M depends on local environments, or the prescription is not more accurate than simply assuming a constant D/M. Studies have shown that at $12 + \log(\mathrm{O/H}) > 8.2$, the D/M falls in the range[16] between 0.4 and 0.7, e.g., 0.5 (Jenkins 2009, taking $F_\star = 1$), 0.72 (Leroy et al. 2011), 0.46 (Rémy-Ruyer et al. 2014), 0.68 (Draine et al. 2014), 0.7 (Feldmann 2015), 0.56 (Chiang et al. 2018), and 0.40–0.58 (Chiang et al. 2021). Meanwhile, studies have shown that in galaxy centers, α_{CO} can vary by a factor of 10 (Bolatto et al. 2013; Sandstrom et al. 2013; Israel 2020; Teng et al. 2022, 2023), which is a significantly larger dynamic range than D/M. In the following, we will take a constant D/M = 0.55 (mean of 0.4–0.7) as the fiducial case for deriving α_{CO}. A possible drawback of assuming a constant D/M is that D/M has been shown to decrease toward lower metallicities (e.g., Hirashita & Kuo 2011; Rémy-Ruyer et al. 2014; Chiang et al. 2018; De Vis et al. 2019). Thus, the assumed D/M value that is appropriate for galaxy centers is likely too high for low-metallicity regions (usually the outer disks), resulting in an underestimation of α_{CO} (Equation (4)) in the outer disk. We will discuss the case of a varying D/M with a toy model in the Appendix. We will also discuss the possible uncertainties in the Σ_{dust} derivation in Section 3.

2.1. CO (1–0) and CO (2–1) Cases

In this multiwavelength, multigalaxy study, we do not always have both the lowest-J CO emission lines for all the target galaxies. Studies have been using CO line ratios to convert the intensity between CO emission lines. For an in-depth discussion on low-J CO line ratios, we refer the readers to Leroy et al. (2022). In the literature, perhaps the most frequently used method to treat different CO line coverage is converting everything to $W_{CO\,(1-0)}$ with a constant CO line ratio (e.g., Sandstrom et al. 2013; Sun et al. 2020; Chiang et al. 2021). This method allows us to uniformly use $\alpha_{CO\,(1-0)}$ for calculating Σ_{mol} in the study. Theoretically, the line ratio can vary with excitation conditions like gas temperature and line width. Thus, we expect R_{21} to trace the local environmental conditions. Taking the line ratio for $W_{CO\,(1-0)}$ and $W_{CO\,(2-1)}$ as an example:

$$R_{21} \equiv \frac{W_{CO\,(2-1)}}{W_{CO\,(1-0)}}, \tag{5}$$

where R_{21} usually falls in the range of 0.3–0.9 with a mean value ~0.65 for normal star-forming galaxies, and it is expected to be higher in galaxy centers (Leroy et al. 2009b; den Brok et al. 2021; Yajima et al. 2021; Leroy et al. 2022, 2023).

[15] The lower bound of the propagated uncertainty likely results from the adopted uncertainty in metallicity.

[16] For studies that only measure D/G measurements, we quote the D/M value calculated at $Z_\odot$.

Table 1
Galaxy Sample

Galaxy (1)	Dist. (Mpc) (2)	i (deg) (3)	P.A. (deg) (4)	R_{25} (kpc) (5)	R_e (kpc) (6)	$\log(M_\star)$ ($M_\odot$) (7)	Type (8)	CO (1–0) (9)	CO (2–1) (10)	HI Ref (11)	12+log(O/H) Ref (12)
IC0342	3.5	31.0	42.0	10.1	4.4	10.2	5	CO Atlas	⋯	EveryTHINGS	*f.*
NGC0253	3.7	75.0	52.5	14.4	4.7	10.5	5	CO Atlas	PHANGS-ALMA	*c.*	*g.*
NGC0300	2.1	39.8	114.3	5.9	2.0	9.3	6	⋯	PHANGS-ALMA	*d.*	*h.*
NGC0598	0.9	55.0	201.0	8.1	2.4	9.4	5	⋯	*a.*	*e.*	*h.*
NGC0628	9.8	8.9	20.7	14.1	3.9	10.2	5	COMING	PHANGS-ALMA	THINGS	PHANGS-MUSE
NGC2841	14.1	74.0	153.0	14.2	5.4	10.9	3	COMING	⋯	THINGS	*g.*
NGC3184	12.6	16.0	179.0	13.6	5.3	10.3	5	CO Atlas	HERACLES	THINGS	*h.*
NGC3198	13.8	72.0	215.0	13.0	5.0	10.0	5	COMING	HERACLES	THINGS	*g.*
NGC3351	10.0	45.1	193.2	10.5	3.1	10.3	3	CO Atlas	PHANGS-ALMA	THINGS	PHANGS-MUSE
NGC3521	13.2	68.8	343.0	16.0	3.9	11.0	3	CO Atlas	PHANGS-ALMA	THINGS	*g.*
NGC3596	11.3	25.1	78.4	6.0	1.6	9.5	5	⋯	PHANGS-ALMA	EveryTHINGS	*g.*
NGC3621	7.1	65.8	343.8	9.9	2.7	10.0	6	⋯	PHANGS-ALMA	THINGS	*h.*
NGC3627	11.3	57.3	173.1	16.9	3.6	10.7	3	CO Atlas	PHANGS-ALMA	THINGS	PHANGS-MUSE
NGC3631	18.0	32.4	−65.6	9.7	2.9	10.2	5	CO Atlas	*b.*	EveryTHINGS	*g.*
NGC3938	17.1	14.0	195.0	13.4	3.7	10.3	5	COMING	HERACLES	HERACLES-VLA	*g.*
NGC3953	17.1	61.5	12.5	15.2	5.3	10.6	4	⋯	*b.*	EveryTHINGS	*g.*
NGC4030	19.0	27.4	28.7	10.5	2.1	10.6	4	COMING	⋯	EveryTHINGS	*g.*
NGC4051	17.1	43.4	−54.8	14.7	3.7	10.3	3	CO Atlas	*b.*	EveryTHINGS	*g.*
NGC4207	15.8	64.5	121.9	3.5	1.4	9.6	7	⋯	PHANGS-ALMA	PHANGS-VLA	*g.*
NGC4254	13.1	34.4	68.1	9.6	2.4	10.3	5	CO Atlas	PHANGS-ALMA	HERACLES-VLA	PHANGS-MUSE
NGC4258	7.6	68.3	150.0	18.8	5.9	10.7	4	COMING	⋯	HALOGAS	*h.*
NGC4321	15.2	38.5	156.2	13.5	5.5	10.7	3	CO Atlas	PHANGS-ALMA	HERACLES-VLA	PHANGS-MUSE
NGC4450	16.8	48.5	−6.3	13.3	4.3	10.7	2	⋯	*b.*	EveryTHINGS	*g.*
NGC4501	16.8	60.1	−37.8	21.1	5.2	11.0	3	CO Atlas	⋯	EveryTHINGS	*g.*
NGC4536	16.2	66.0	305.6	16.7	4.4	10.2	3	CO Atlas	PHANGS-ALMA	HERACLES-VLA	*g.*
NGC4569	15.8	70.0	18.0	21.0	5.9	10.8	2	CO Atlas	PHANGS-ALMA	HERACLES-VLA	*g.*
NGC4625	11.8	47.0	330.0	2.4	1.2	9.1	9	⋯	HERACLES	HERACLES-VLA	*h.*
NGC4651	16.8	50.1	73.8	9.5	2.4	10.3	5	⋯	*b.*	EveryTHINGS	*h.*
NGC4689	15.0	38.7	164.1	8.3	4.7	10.1	5	CO Atlas	PHANGS-ALMA	EveryTHINGS	*g.*
NGC4725	12.4	54.0	36.0	17.5	6.0	10.8	1	⋯	HERACLES	HERACLES-VLA	*g.*
NGC4736	4.4	41.0	296.0	5.0	0.8	10.3	1	CO Atlas	HERACLES	THINGS	*g.*
NGC4941	15.0	53.4	202.2	7.3	3.4	10.1	1	⋯	PHANGS-ALMA	EveryTHINGS	*g.*
NGC5055	9.0	59.0	102.0	15.5	4.2	10.7	4	CO Atlas	HERACLES	THINGS	*g.*
NGC5248	14.9	47.4	109.2	8.8	3.2	10.3	3	CO Atlas	PHANGS-ALMA	PHANGS-VLA	*g.*
NGC5457	6.7	18.0	39.0	23.4	13.5	10.3	5	CO Atlas	HERACLES	THINGS	*h.*
NGC6946	7.3	33.0	243.0	12.1	4.4	10.5	5	CO Atlas	HERACLES	THINGS	*h.*
NGC7331	14.7	76.0	168.0	19.8	3.7	11.0	4	COMING	HERACLES	THINGS	*g.*

Notes. (2) Distance (from EDD Tully et al. 2009); (3)–(4) inclination angle and position angle (Sofue et al. 1999; De Blok et al. 2008; Leroy et al. 2009b; Meidt et al. 2009; Muñoz-Mateos et al. 2009; McCormick et al. 2013; Makarov et al. 2014; Lang et al. 2020); (5) isophotal radius (Makarov et al. 2014); (6) effective radius (Leroy et al. 2021); (7) logarithmic global stellar mass (Leroy et al. 2019); (8) numerical Hubble stage T; (9) References of CO $J = 1 \rightarrow 0$ observations ("⋯" means no CO $J = 1 \rightarrow 0$ data adopted in this work): CO Atlas Kuno et al. (2007); COMING (Sorai et al. 2019); (10) References of CO $J = 2 \rightarrow 1$ observations ("⋯" means no CO $J = 2 \rightarrow 1$ data adopted in this work): HERACLES Leroy et al. (2009b); PHANGS-ALMA (Leroy et al. 2021); *a.* M33 data from Gratier et al. (2010); Druard et al. (2014); *b.* New HERA data (P.I.: A. Schruba; presented in Leroy et al. 2022); (11) References of HI observations: THINGS (Walter et al. 2008); HALOGAS (Heald et al. 2011); HERACLES-VLA (Schruba et al. 2011); PHANGS-VLA (P.I. D. Utomo; I. Chiang et al. 2024, in preparation); EveryTHINGS (P.I. K. M. Sandstrom; I. Chiang et al. 2024, in preparation); *c.* Puche et al. (1991); *d.* Puche et al. (1990); *e.* Koch et al. (2018); (12) References of 12 + log(O/H) measurement: PHANGS-MUSE (Emsellem et al. 2022; Santoro et al. 2022); *f.* private communication with K. Kreckel (see Chiang et al. 2021); *g.* using the empirical formula described in Section 3.1; *h.* data from Zurita et al. (2021) compilation.

In this work, however, we will not adopt the simple strategy as our fiducial case because most of our target galaxies have CO (2–1) data, that $\alpha_{CO\,(2-1)}$ has attained its own importance due to modern observations, and that the variation in R_{21} is nonnegligible. We will present four solutions of α_{CO} in parallel, two without any conversions between CO (2–1) and CO (1–0), and two with different prescriptions of the line ratio:

1. $\alpha_{CO\,(2-1)}$ calculated with $W_{CO\,(2-1)}$ data only.
2. $\alpha_{CO\,(1-0)}$ calculated with $W_{CO\,(1-0)}$ data only.
3. $\alpha_{CO\,(1-0)}$ calculated with $W_{CO\,(1-0)}$ data, plus $W_{CO\,(2-1)}$ for galaxies without $W_{CO\,(1-0)}$ data, converted with a constant R_{21}.
4. $\alpha_{CO\,(1-0)}$ calculated with $W_{CO\,(1-0)}$ data, plus $W_{CO\,(2-1)}$ for galaxies without $W_{CO\,(1-0)}$ data, converted with an environment-dependent R_{21}.

For the third method, we adopt the constant $R_{21} = 0.65$ from Leroy et al. (2022). For the last method, we adopt the mid-infrared (MIR)-dependent formula suggested by

Leroy et al. (2023), namely,

$$R_{21} = 0.62\left(\frac{I_{\rm WISE4}}{1\ {\rm MJy\ sr^{-1}}}\right)^{0.22}. \quad (6)$$

We follow the suggestion in Leroy et al. (2023) and cap R_{21} at $R_{21} = 1$. This formula, in general, agrees with the finding that R_{21} scales with MIR intensity or $\Sigma_{\rm SFR}$ with a power-law index of ∼0.15–0.2 (den Brok et al. 2021; Yajima et al. 2021; Leroy et al. 2022, 2023).

3. Data

We measure $\alpha_{\rm CO}$ in 37 nearby galaxies in this study. To measure $\alpha_{\rm CO}$ with our dust-based methodology (Section 2), the data sets required are dust surface density ($\Sigma_{\rm dust}$, from IR SED modeling), CO low-J rotational line integrated intensity ($W_{\rm CO}$), atomic gas surface density ($\Sigma_{\rm atom}$, from H I 21 cm line emission), and metallicity (Z, from gas-phase oxygen abundance in H II regions). We first select our sample galaxies from the dust catalog of $z = 0$ Multiwavelength Galaxy Synthesis (z0MGS; Leroy et al. 2019; Chastenet et al. 2021, J. Chastenet et al. 2024, in preparation). From this large sample, we pick the 49 galaxies with both low-J CO rotational line and H I data available, including our own new H I data sets. We design our study with a common resolution of 2 kpc, which draws a limit in sample selection at distance ∼20 Mpc as the worst resolution data in our sample usually have angular resolution around 20″. High-inclination (>80°) targets are also excluded. We further exclude four galaxies[17] that satisfy all the above conditions but do not satisfy the signal-to-noise ratio (S/N) conditions that will be described in Section 3.3. The selection yields 37 galaxies in our sample. We list the properties of these galaxies in Table 1.

3.1. Physical Quantities and Data Sets

Dust properties. We obtain the dust properties by fitting the dust emission SED to the Draine & Li (2007) physical dust model. The details of the IR data processing and dust SED fitting are reported in Chastenet et al. (2021) and J. Chastenet et al. (2024, in preparation). We briefly summarize the process below.

We obtain the dust emission SED in the IR observed by two space telescopes: the 3.4, 4.6, 12, and 22 μm bands with WISE (Wright et al. 2010), and the 70, 100, 160, and 250 μm bands with the Herschel Space Observatory (Pilbratt et al. 2010). The Herschel and WISE maps are first convolved to SPIRE 250 point-spread function (PSF) and then to a 21″ Gaussian PSF using the SPIRE 250-to-Gauss-21″ kernel from Aniano et al. (2011). The 21″ PSF is the "moderate" Gaussian from Aniano et al. (2011) that provides relatively high angular resolution without amplifying image artifacts. Finally, these maps are convolved to the desired resolution: a Gaussian PSF with spatial resolution corresponding to FWHM of 2 kpc.

After convolving the IR maps, we fit the dust SED with the Draine & Li (2007) physical dust model with the dust opacity calibration derived in Chastenet et al. (2021). This calibration is based on metallicity measured with "direct" electron-temperature-based methods, which is consistent with the strong line calibration adopted in this work (S-calibration in Pilyugin & Grebel 2016) and yields reasonable D/M. Thus, the calibration ties the dust opacity, D/M, and metallicity into one framework. The complete set of data products from the fitting includes the maps of the dust-mass surface density ($\Sigma_{\rm dust}$), interstellar radiation field (the minimum radiation field $U_{\rm min}$ and the fraction of dust heated by the power-law radiation field γ), and the fractional dust mass in the form of polycyclic aromatic hydrocarbons ($q_{\rm PAH}$). The maximum radiation field is fixed at $U_{\rm max} = 10^7$, and the power-law index for radiation field distribution is fixed at $\alpha = 2$. From the fitted $U_{\rm min}$ and γ, we can derive the dust-mass-averaged radiation field $\overline{U}$, which is the fiducial tracer for the radiation field in this work.

We also note that we assume fixed dust properties in our dust SED fitting throughout this study, which is the most frequently adopted strategy in the literature. The accuracy of $\Sigma_{\rm dust}$ estimates, derived by fitting the IR SED with dust emission models, can be affected by variations in the dust opacity. Interstellar dust grains are not uniform in their chemical composition, size distribution, and shape, leading to variations in their opacity (e.g., Draine & Li 2007; Hirashita & Voshchinnikov 2014; Draine & Hensley 2021). In the MW, Stepnik et al. (2003) found that the dust opacity increases by ∼3 times from the diffuse ISM to the dense clouds. The authors argued that the increase in dust opacity resulted from the deficit of small grains due to grain–grain coagulation. It is challenging to measure the variation in opacity of interstellar dust as it degenerates with the environmental dependence of $\alpha_{\rm CO}$ and D/M. Moreover, many of the mechanisms that affect the dust opacity, e.g., grain–grain coagulation and ice mantles, are smoothed out in kpc-scale extragalactic studies (Galliano et al. 2018), meaning that its variation is likely less observable than the other degenerate factors like $\alpha_{\rm CO}$ and D/M. We note that there are extragalactic studies that attribute all the variations in dust and gas properties to dust opacity to evaluate its variation; e.g., Clark et al. (2019) found that the dust opacity changes by a factor ∼2 within M74 and ∼5 within M83.

Atomic gas surface density. We trace the atomic gas surface density ($\Sigma_{\rm atom}$) with the H I 21 cm integrated intensity ($I_{\rm H\,I}$), assuming the opacity is negligible (e.g., Walter et al. 2008):

$$\frac{\Sigma_{\rm atom}}{1\ M_\odot\ {\rm pc^{-2}}} = 1.36 \times (1.46 \times 10^{-2}) \times \frac{W_{\rm H\,I}}{1\ {\rm K\ km\ s^{-1}}}, \quad (7)$$

where the 1.36 factor accounts for the mass of helium.

We obtain $W_{\rm H\,I}$ from both literature and new data, as listed in Table 1. The two new H I surveys are the EveryTHINGS survey (P.I. K. M. Sandstrom; I. Chiang et al. 2024, in preparation) and the PHANGS Very Large Array (VLA) survey (P.I. D. Utomo). The EveryTHINGS survey targets nearby galaxies with Herschel photometric data but without high-resolution H I observations, while the PHANGS-VLA survey focuses on galaxies in the PHANGS project.[18] Both surveys have their data observed with the C and D configurations of the Karl G. Jansky VLA,[19] which yield angular resolutions in the range of 20″–30″. Both surveys provide new high-sensitivity 21 cm H I observations in tens of nearby galaxies. We did not include WHISP (Swaters et al. 2002) data because the galaxies that only have WHISP data have a resolution coarser than 2 kpc after convolving to a circular PSF.

[17] NGC 925, NGC 2403, NGC 4496A, and NGC 7793.

[18] http://phangs.org/

[19] The VLA is operated by the National Radio Astronomy Observatory (NRAO), which is a facility of the National Science Foundation operated under a cooperative agreement by Associated Universities, Inc.

CO low-J rotational lines. The integrated intensity of CO low-J rotational lines traces the molecular gas surface density (Equation (1)) and is key to this study. We use the compilation of CO mapping assembled by Leroy et al. (2022, 2023) from several publicly available CO (1–0) and CO (2–1) data:

1. CO (1–0) data from the COMING survey (Sorai et al. 2019) and the CO Atlas (Kuno et al. 2007).
2. CO (2–1) data from HERACLES (Leroy et al. 2009b), the PHANGS-ALMA survey (Leroy et al. 2021), and a new survey observed by the IRAM 30 m focused on the Virgo Cluster (P.I. A. Schruba; processed in Leroy et al. 2022).

The source of CO data for each galaxy is listed in Table 1, where CO (1–0) and CO (2–1) are listed separately. All these literature measurements focus on the $^{12}C^{16}O$ isotopologue, hereafter CO for simplicity.

Surface densities of stellar mass and star formation rate (SFR). We trace the surface densities of stellar mass and SFR ($\Sigma_\star$ and $\Sigma_{\rm SFR}$, respectively) using the data and conversion formulae presented in the z0MGS survey (Leroy et al. 2019). We utilize the z0MGS compilation of the background-subtracted WISE (Wright et al. 2010) $\lambda \sim 3.4$ and 22 μm (hereafter WISE1 and WISE4, respectively) data and the Galaxy Evolution Explorer (GALEX; Martin et al. 2005) $\lambda \sim 154$ nm (hereafter FUV) data.

We use WISE1 data to trace stellar mass surface density ($\Sigma_\star$) with:

$$\frac{\Sigma_\star}{1\ M_\odot\ \mathrm{pc^{-2}}} = 3.3 \times 10^2 \left(\frac{\Upsilon_\star^{3.4}}{0.5\ M_\odot\ L_\odot^{-1}}\right) \frac{I_{\rm WISE1}}{1\ \mathrm{MJy\ sr^{-1}}}, \quad (8)$$

where $\Upsilon_\star^{3.4}$ is the $\Sigma_\star$-to-WISE1 mass-to-light ratio. The value of $\Upsilon_\star^{3.4}$ is calculated from the galaxy-by-galaxy SFR-to-WISE1 ratio, a "specific SFR-like" quantity, with the prescription calibrated in Appendix A of Leroy et al. (2019).

We use FUV and WISE4 data to trace the SFR surface density ($\Sigma_{\rm SFR}$) also with the conversion formula suggested by z0MGS (Leroy et al. 2019; Belfiore et al. 2023). For galaxies with both FUV and WISE4 available, we use:

$$\frac{\Sigma_{\rm SFR}}{1\ M_\odot\ \mathrm{yr^{-1}\,kpc^{-2}}} = 8.85 \times 10^{-2} \frac{I_{\rm FUV}}{1\ \mathrm{MJy\ sr^{-1}}} + 3.02 \times 10^{-3} \frac{I_{\rm WISE4}}{1\ \mathrm{MJy\ sr^{-1}}}. \quad (9)$$

For NGC3953 and NGC4689, where only WISE4 is available, we use:

$$\frac{\Sigma_{\rm SFR}}{1\ M_\odot\ \mathrm{yr^{-1}\,kpc^{-2}}} = 3.81 \times 10^{-3} \frac{I_{\rm W4}}{1\ \mathrm{MJy\ sr^{-1}}}. \quad (10)$$

For both WISE and GALEX maps, we blank the regions with foreground stars identified in the z0MGS database. We interpolate the intensities in the blanked region with a Gaussian kernel FWHM = 22.″5 (the adopted WISE and GALEX maps have FWHM = 15″) with the function `interpolate_replace_nans` in `astropy.convolution`. This interpolation is done on the maps before any convolution, reprojection, or unit conversion. Regarding the WISE maps, this treatment is only done for the maps used for calculating $\Sigma_\star$ and $\Sigma_{\rm SFR}$. For the WISE maps used in dust SED fitting, we refer the readers to J. Chastenet et al. (2024, in preparation).

Specific SFR. With the measurements of $\Sigma_{\rm SFR}$ and $\Sigma_\star$, we calculate the specific SFR (sSFR) as:

$$\frac{\rm sSFR}{1\ \mathrm{yr^{-1}}} = 1 \times 10^{-6} \times \left(\sum_i \frac{\Sigma_{\rm SFR}}{1\ M_\odot\ \mathrm{yr^{-1}\,kpc^{-2}}}\right)\left(\sum_i \frac{\Sigma_\star}{1\ M_\odot\ \mathrm{pc^{-2}}}\right)^{-1}, \quad (11)$$

where $\sum_i$ is the summation over pixels in a galaxy. Meanwhile, we calculate the spatially resolved sSFR (rsSFR) as:

$$\frac{\rm rsSFR}{1\ \mathrm{yr^{-1}}} = 1 \times 10^{-6} \times \frac{\Sigma_{\rm SFR}}{1\ M_\odot\ \mathrm{yr^{-1}\,kpc^{-2}}}\left(\frac{\Sigma_\star}{1\ M_\odot\ \mathrm{pc^{-2}}}\right)^{-1}. \quad (12)$$

Metallicity. We use the abundance of oxygen, 12 + log(O/H), to trace the metallicity (Z). We assume a fixed abundance pattern, i.e., a constant oxygen-to-total-metal mass ratio. The conversion from 12 + log(O/H) to Z then becomes:

$$Z = 0.0134 \times 10^{12+\log(\mathrm{O/H})-8.69}, \quad (13)$$

where 0.0134 and 8.69 are the adopted $Z_\odot$ and $12 + \log(\mathrm{O/H})_\odot$, respectively (Asplund et al. 2009).

We calculate 12 + log(O/H) for each pixel as a function of the galactocentric distance by adopting the radial gradient of 12 + log(O/H) derived from measurements in H II regions. We use data from two surveys: the PHANGS-MUSE survey (Emsellem et al. 2022; Groves et al. 2023) and the Zurita et al. (2021) compilation. We use the Pilyugin & Grebel (2016) S-calibration[20] (hereafter PG16S) as the fiducial calibration for 12 + log(O/H). PG16S is a calibration method that shows good agreement with direct metallicity measurements (Croxall et al. 2016; Kreckel et al. 2019). As PG16S only relies on lines covered by MUSE, the 12 + log(O/H) measurement can be expanded to the full PHANGS-MUSE data set in our future works.

For galaxies in the PHANGS-MUSE survey, we adopt radial 12 + log(O/H) gradients presented in Santoro et al. (2022), which are calculated with the PG16S calibration. For galaxies that only appear in the Zurita et al. (2021) emission data compilation, we use the Zurita et al. (2021) data to calculate the PG16S 12 + log(O/H) and then fit the radial 12 + log(O/H) gradient in these galaxies. We only consider galaxies that have at least five measurements spanning at least $0.5R_{25}$ in the Zurita et al. (2021) data table. The uncertainties in the 12 + log(O/H) gradient are not explicitly provided in either work. We will assume a 0.1 dex scatter for 12 + log(O/H) derived from gradients, as suggested in Berg et al. (2020).

For galaxies without measurements of 12 + log(O/H) in either Zurita et al. (2021) or Santoro et al. (2022), we use the two-step strategy proposed in Sun et al. (2020) to estimate their 12 + log(O/H). First, we use a mass–metallicity relation to predict 12 + log(O/H) at one effective radius ($R_{\rm e}$) in a given galaxy. Second, we extend the prediction with a radial gradient of -0.1 dex$/R_{\rm e}$ suggested by Sánchez et al. (2014). We

[20] Pilyugin & Grebel (2016) utilizes the $S_2 = I_{[\rm S\,II]}\lambda6717 + \lambda6731/I_{\rm H\beta}$, $N_2 = I_{[\rm N II]}\lambda6548 + \lambda6584/I_{\rm H\beta}$, and $R_3 = I_{[\rm O III]}\lambda4959 + \lambda5007/I_{\rm H\beta}$ line ratios to measure gas-phase 12 + log(O/H).

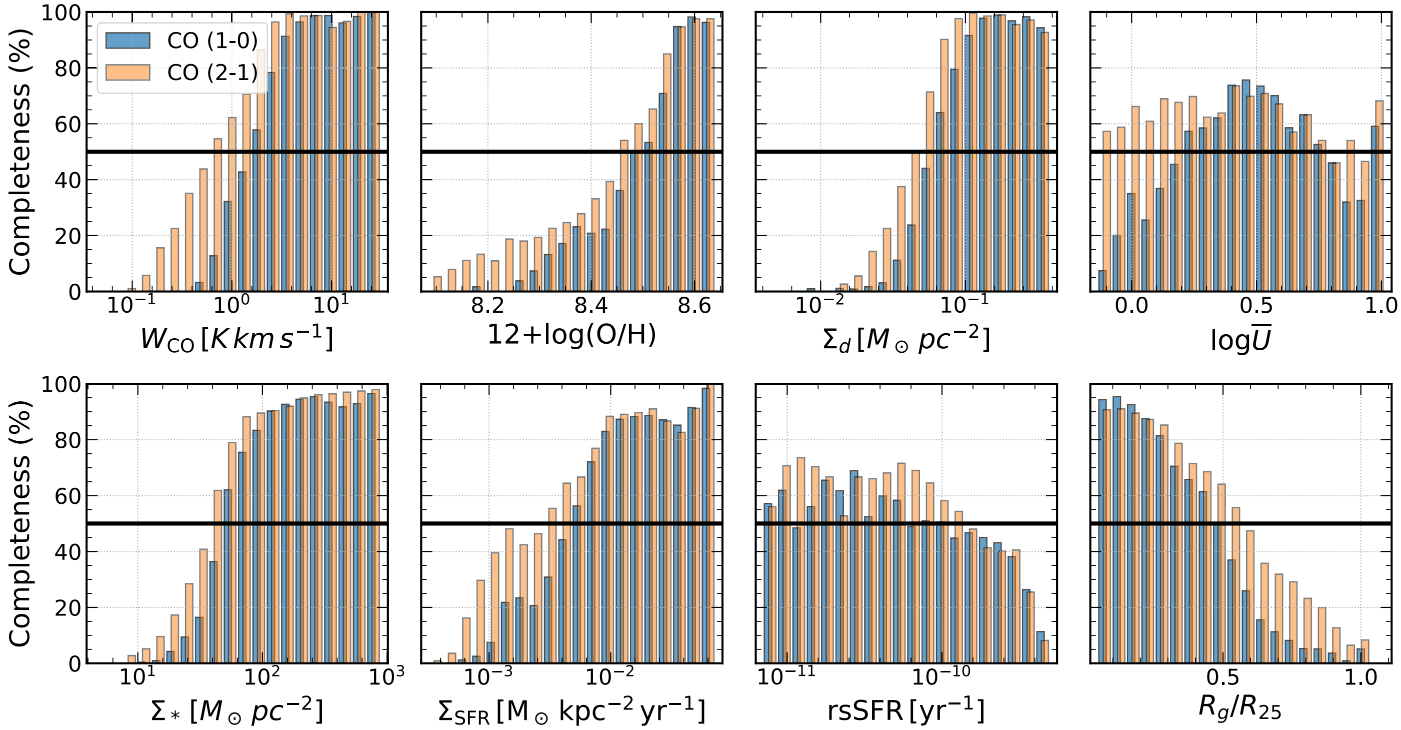

Figure 1. Completeness of our data set at each α_{CO}-quantity pair. The 50% completeness is marked with a horizontal black line. In the statistical calculations, e.g., linear regression and correlation, we only use data in the parameter range with completeness >50%.

characterize the mass–metallicity with a function of the form:

$$12 + \log(O/H) = a + bxe^{-x}, \tag{14}$$

where $x = \log(M_\star/M_\odot) - 11.5$ (see Sánchez et al. 2019, and references therein). a and b are free parameters. We fit the function with $12 + \log(O/H)$ at one R_e from galaxies with the available measurements listed in Table 1. The best-fit parameters are $a = 8.56 \pm 0.02$ and $b = 0.010 \pm 0.002$, which are robust under resampling. Meanwhile, the typical statistical uncertainty in the $12 + \log(O/H)$ data used for fitting is ~0.013 dex. However, the rms error (Δ_{rms}) between the best fit and data is 0.13 dex, meaning that there is still intrinsic scatter in $12 + \log(O/H)$ that is not explained by the mass–metallicity relation and the adopted radial gradients, e.g., the azimuthal variations (Williams et al. 2022). We use this fitted relation to derive the radial metallicity gradient of galaxies without metallicity measurements with the $M_\star$ and R_e listed in Table 1. We will assume an uncertainty of 0.15 dex (rounding up $0.013 + 0.13$ dex) for galaxies with this type of $12 + \log(O/H)$ measurements.

Studies have reported that the PG16S calibration could result in $12 + \log(O/H)$ value lower than other calibrations (e.g., De Vis et al. 2019). Aligning with that, there are also studies reporting that the $12 + \log(O/H)$ calibrated with PG16S in Orion Nebula and other H II regions in the solar neighborhood have values ~0.2 dex lower than the solar reference value (e.g., Esteban et al. 2022). This effect could lead to an underestimate of Z' and thus an overestimate in α_{CO} with our methodology. For consistency with the direct metallicity calibration used in Chastenet et al. (2021) for calibrating dust opacity, we will use PG16S in this work.

3.2. Uniform Data Processing

The analyses in this work are done at a common resolution of 2 kpc for all data. For H I, CO, $\Sigma_\star$, and Σ_{SFR}, we convolve them to a circular Gaussian PSF with a FWHM corresponding to 2 kpc, using the `astropy.convolution` package (Astropy Collaboration et al. 2013, 2018, 2022). The images are then reprojected onto a grid with a pixel size of one-third of the FWHM (that is, we oversample at roughly the Nyquist sampling rate) with the `astropy`-affiliated package `reproject`. The convolution and reprojection of the dust maps are done in J. Chastenet et al. (2024, in preparation). They convolve the IR maps into the final resolution using kernels from Aniano et al. (2011). Note that the convolution is done before SED fitting for dust properties. The galactocentric radius and metallicity are directly calculated on the final pixel grids. All the surface density and surface brightness quantities presented in this work have been corrected for inclination, as listed in Table 1.

3.3. S/N Mask and Completeness

S/N Mask. For statistical quantities that only involve α_{CO}, e.g., mean values and percentiles, we masked out low-S/N pixels. In particular, we blank pixels with $S/N < 1$ in W_{CO} and Σ_{mol}. Note that Σ_{mol} here is derived from Σ_{dust} (with IR photometry), metallicity, and Σ_{atom} (Equation (4)); thus the uncertainty in Σ_{mol} is propagated from the uncertainties in these three quantities and the IR photometry.

Completeness. For statistical quantities that involve α_{CO} and another quantity (X), e.g., correlations and linear regression, in addition to the S/N mask, we only calculate with data with high (>50%) completeness in X as the trend confidence criteria. The completeness for data with $X_i \leqslant X < X_f$, or $[X_i, X_f)$,

Table 2
Statistics of $\alpha_{\rm CO}$ Measurements

Galaxy	$\alpha_{\rm CO\,(2-1)}$						$\alpha_{\rm CO\,(1-0)}$					
	Mean	W-mean[a]	16th–84th %tile[b]	$W_{\rm CO}$%[c]	$N_{\rm pix}$[d]	$N_{\rm pix,100}$[e]	Mean	W-mean[a]	16th–84th %tile[b]	$W_{\rm CO}$%[c]	$N_{\rm pix}$[d]	$N_{\rm pix,100}$[e]
IC0342	⋯	⋯	⋯	⋯	⋯	⋯	2.62	2.31	1.46–4.41	100.0%	168	28
NGC0253	14.15	5.16	3.55–28.62	99.7%	108	37	2.47	1.99	1.26–4.25	100.0%	39	31
NGC0300	13.42	13.41	5.66–33.33	100.0%	5	0	6.64[f]	6.63[f]	2.74–15.59[f]	100.0%	5[f]	0[f]
NGC0598	10.58	10.05	4.29–24.69	65.2%	41	0	5.93[f]	5.76[f]	2.44–13.76[f]	65.2%	41[f]	0[f]
NGC0628	6.69	6.63	4.25–10.17	100.0%	172	57	3.31	3.32	1.68–6.24	66.8%	172	57
NGC2841	⋯	⋯	⋯	⋯	⋯	⋯	9.51	9.15	3.73–22.03	75.5%	131	92
NGC3184	4.12	4.11	2.09–7.68	57.2%	267	56	2.44	2.41	1.13–4.95	87.3%	247	56
NGC3198	4.92	4.37	1.7–12.59	22.4%	19	0	2.63	2.28	0.81–7.49	26.6%	18	0
NGC3351	7.29	5.41	3.94–11.71	100.0%	82	54	2.92	2.84	1.49–5.63	62.7%	81	54
NGC3521	8.68	6.7	3.58–17.2	92.8%	206	143	4.06	3.67	1.87–8.0	96.0%	162	125
NGC3596	11.14	9.99	6.19–18.28	100.0%	40	16	7.81[f]	7.32[f]	4.59–12.63[f]	100.0%	40[f]	16[f]
NGC3621	5.53	5.45	2.99–10.05	98.6%	52	19	3.96[f]	4.01[f]	2.15–7.19[f]	98.6%	52[f]	19[f]
NGC3627	4.63	3.84	2.58–7.37	100.0%	176	143	1.87	1.71	1.08–2.96	75.9%	176	143
NGC3631	8.82	5.1	2.53–21.84	29.2%	102	17	3.1	2.55	1.08–7.81	25.3%	97	17
NGC3938	5.91	5.61	2.78–11.7	71.0%	229	88	3.51	3.39	1.58–7.33	78.3%	224	88
NGC3953	15.35	12.27	5.93–32.15	91.7%	483	98	8.27[f]	7.19[f]	3.42–17.22[f]	91.7%	483[f]	98[f]
NGC4030	⋯	⋯	⋯	⋯	⋯	⋯	5.71	4.57	2.68–11.09	93.8%	207	135
NGC4051	13.85	9.79	6.08–24.27	87.9%	394	42	5.44	4.74	2.33–11.2	72.2%	200	36
NGC4207	4.25	4.22	2.2–8.1	100.0%	4	4	3.32[f]	3.31[f]	1.77–6.16[f]	100.0%	4[f]	4[f]
NGC4254	3.93	4.0	2.37–6.43	90.3%	193	89	2.45	2.52	1.34–4.19	77.7%	193	89
NGC4258	⋯	⋯	⋯	⋯	⋯	⋯	2.18	1.73	0.77–5.24	69.6%	56	55
NGC4321	7.37	5.39	4.0–11.94	100.0%	459	199	4.45	3.77	2.64–6.75	99.9%	286	198
NGC4450	8.28	5.27	2.28–18.6	90.0%	144	118	3.81[f]	2.78[f]	1.19–8.46[f]	90.0%	144[f]	118[f]
NGC4501	⋯	⋯	⋯	⋯	⋯	⋯	7.58	6.1	3.44–14.25	98.8%	336	235
NGC4536	4.6	2.0	1.11–11.05	64.8%	35	21	2.08	1.77	0.8–4.01	44.7%	28	21
NGC4569	7.49	3.98	2.41–13.96	100.0%	139	83	4.14	2.88	1.47–8.3	82.7%	127	83
NGC4625	5.79	5.64	2.16–15.71	18.5%	5	0	3.59[f]	3.52[f]	1.29–9.49[f]	18.5%	5[f]	0[f]
NGC4651	4.22	4.15	2.16–7.59	54.4%	39	39	3.36[f]	3.34[f]	1.7–6.04[f]	54.4%	39[f]	39[f]
NGC4689	10.23	8.48	4.75–19.72	99.7%	132	40	4.59	4.24	2.09–9.21	73.3%	124	40
NGC4725	12.68	10.56	4.16–29.68	75.7%	317	146	6.21[f]	5.24[f]	2.01–14.55[f]	75.7%	317[f]	146[f]
NGC4736	2.31	1.87	0.83–5.25	83.7%	30	30	1.26	1.18	0.49–3.01	100.0%	14	14
NGC4941	8.1	7.1	3.1–16.19	69.5%	47	31	4.95[f]	4.75[f]	2.15–9.68[f]	69.5%	47[f]	31[f]
NGC5055	8.94	7.47	4.13–17.65	92.3%	312	120	4.55	4.43	2.46–8.24	100.0%	157	112
NGC5248	11.23	7.02	4.88–19.99	100.0%	218	87	5.08	4.06	2.39–9.52	88.2%	196	87
NGC5457	6.87	6.19	3.47–12.67	87.9%	419	50	3.38	3.16	1.81–6.06	95.6%	311	50
NGC6946	3.27	2.74	1.7–5.91	87.4%	372	121	2.26	1.89	1.14–4.05	96.8%	312	121
NGC7331	19.48	11.17	6.36–42.52	88.3%	345	106	6.41	5.35	2.67–13.69	86.2%	236	105
Overall	9.32	5.69	3.91–13.96	⋯	5586	2054	4.22	3.33	2.21–6.09	⋯	4298	2072
Overall[f]	⋯	⋯	⋯	⋯	⋯	⋯	4.72[f]	3.48[f]	2.32–7.23[f]	⋯	5475[f]	2543[f]

Note. All the $\alpha_{\rm CO}$ Values are in units of $[M_\odot\ {\rm pc}^{-2} ({\rm K\ km\ s}^{-1})^{-1}]$.
[a] CO-intensity-weighted mean.
[b] The percentiles are calculated with nonweighted data.
[c] Fraction of $W_{\rm CO}$ recovered (above the S/N mask) in each galaxy. Galaxies with CO recovery fraction <50% will be visualized differently in figures showing galaxy-averaged values.
[d] Number of pixel-by-pixel measurements.
[e] Number of pixel-by-pixel with valid $\alpha_{\rm CO}$ measurements at $\Sigma_\star \geqslant 100\ M_\odot {\rm pc}^{-2}$. This will be discussed later in Section 5.
[f] $\alpha_{\rm CO\,(1-0)}$ calculated with $R_{21}(I_{\rm W4})$ (Equation (6)) and $W_{\rm CO\,(2-1)}$ due to no $W_{\rm CO\,(1-0)}$ data.

is defined as:

$$\text{Completeness} \equiv \frac{\text{num of S/N} > 1 \text{ pixels with } [X_i,\ X_f)}{\text{num of all pixels with } [X_i,\ X_f)}, \tag{15}$$

where the definition of "S/N > 1" is the same as the S/N mask earlier this subsection. We show the completeness and the 50% threshold in our data set in Figure 1. For most quantities, the CO (2–1) data have a better completeness coverage than the CO (1–0) data. Note that at the high-$\overline{U}$ end, the completeness fluctuates around 50%. We treat all data with $\log \overline{U} > 0.75$ as incomplete for simplicity.

4. Results

In total, we measure resolved $\alpha_{\rm CO}$ values across 37 galaxies, including ∼790 and ∼610 independent measurements[21] from CO (2–1) and CO (1–0) data, respectively. We summarize the measurements in Table 2 and the distribution of $\alpha_{\rm CO}$ in

[21] In our data products, the pixel size is 1/3 of the FWHM of the Gaussian PSF. Thus, the number of independent measurements is smaller than the number of pixels listed in Table 2.

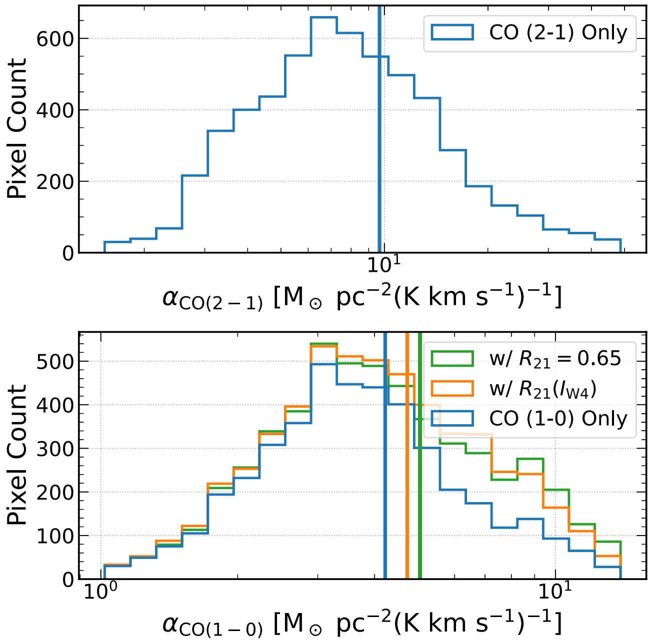

Figure 2. Distribution of measured $\alpha_{CO\,(2-1)}$ and $\alpha_{CO\,(1-0)}$. The mean value of each type of measurement is marked in vertical lines with the corresponding color.

Figure 2. For each galaxy, we report the mean, CO-intensity-weighted mean, 16th–84th percentiles, and number of pixel-by-pixel measurements of α_{CO}.

The mean value for $\alpha_{CO\,(2-1)}$ and $\alpha_{CO\,(1-0)}$ are 9.3 and 4.2 $M_\odot$ pc^{-2}(K km s^{-1})$^{-1}$ with 16th–84th percentiles spanning 3.9–14.0 and 2.2–6.1 $M_\odot$ pc^{-2}(K km s^{-1})$^{-1}$, respectively. The mean $\alpha_{CO\,(1-0)}$ corresponds to $\sim 0.97\alpha_{CO}^{MW}$, whereas the mean $\alpha_{CO\,(2-1)}$ corresponds to $\sim 1.39\alpha_{CO}^{MW}$ assuming a constant $R_{21}=0.65$.

Besides the simple mean, we also calculate the W_{CO}-weighted mean, which better reflects the α_{CO} value to be adopted for data at coarser resolution. The W_{CO}-weighted mean for $\alpha_{CO\,(2-1)}$ and $\alpha_{CO\,(1-0)}$ are 5.69 and 3.33, respectively. Both values are lower than the simple mean, which indicates that the α_{CO} values are lower in brighter regions. Unless specified otherwise, we use W_{CO}-weighted mean α_{CO} for galaxy-integrated analysis in the following content.

When we include CO (2–1) data for galaxies without CO (1–0) measurements with a variable R_{21} (values with † in Table 2), the mean and W_{CO}-weighted mean of $\alpha_{CO\,(1-0)}$ increase to 4.72 and 3.48, respectively, indicating that galaxies without CO (1–0) measurements in this data set tend to have larger α_{CO}. This is also visualized in the bottom panel of Figure 2. Also, we find that the distribution of $\alpha_{CO\,(1-0)}$ does not differ much between the two R_{21} prescriptions adopted in this work: the fixed $R_{21}=0.65$ and the I_{W4}-dependent R_{21}.

In Table 2, we also list the W_{CO} recovery fraction (W_{CO}%), which is the percentage of W_{CO} recovered (above the S/N mask) in the pixel-by-pixel analysis in each galaxy. We notice a few galaxies with low W_{CO} recovery fractions, meaning that there are significant numbers of pixels with W_{CO} detection removed from the analysis. The main reason for NGC3631 and most galaxies with recovery fraction above 50% is low sensitivity in dust/IR data. In NGC3631, >85% of pixels removed have $S/N < 1$ in the IR bands. In NGC3198 and NGC4625, the sensitivity in dust/IR only explains <60% of pixels removed. The rest of the pixels were removed due to $S/N < 1$ in Σ_{mol}, a combined effect of Σ_{dust}, Σ_{atom}, and $12+\log(O/H)$. This type of pixel has $S/N > 1$ in W_{CO} and $S/N < 1$ in Σ_{mol}, likely indicating a small α_{CO}.

4.1. Correlations with Local Conditions

We measure the pixel-by-pixel correlations between α_{CO} and several parameters describing local physical conditions. These results are summarized in Table 3 and visualized in Figures 3–4. Note that the correlations and linear regressions[22] are calculated with data in the complete zone only (with data completeness >50%; see Section 3.3 for details). The error bars in Figures 3–4 include both the scatter within a bin and the uncertainties in pixel-by-pixel measurements. We first bootstrap the measurements by 1000 times with uncertainties and then sample the 16th and 84th percentiles in each bin from the bootstrapped sample as the error bars. We apply the same method for visualizing the other binned data in this work.

As shown in Table 3, most quantities have significant correlations (p-value <0.05) with α_{CO} except $\Sigma_\star$. $\Sigma_\star$ has significant correlations with $\alpha_{CO\,(2-1)}$ from CO (2–1) data only and $\alpha_{CO\,(1-0)}$f from CO (1–0) only, but not when we combine CO (2–1) and CO (1–0) data. This is likely due to the negative $\Sigma_\star$-to-$\alpha_{CO\,(2-1)}$ and the positive $\Sigma_\star$-to-$\alpha_{CO\,(1-0)}$ correlations, although both of which are weak.

$\log \overline{U}$ has the strongest negative correlation with $\alpha_{CO\,(2-1)}$, meaning that $\alpha_{CO\,(2-1)}$ decreases toward regions with stronger interstellar radiation field strength. This is consistent with the picture that α_{CO} decreases with higher gas temperature and larger line width (Bolatto et al. 2013). It is also the case that a higher $\log \overline{U}$ might correspond to a lower Σ_{dust} as a caveat of our fitting methodology (equivalent to "fixing β" in modified blackbody models; see Shetty et al. 2009a, 2009b). However, as we do not see a strong Σ_{dust}-to-$\alpha_{CO\,(2-1)}$ correlation, the above effect should be minor. Several other quantities also show moderate (negative) correlations with $\alpha_{CO\,(2-1)}$, i.e., Σ_{SFR} and rsSFR. Studies have shown strong correlations between $\log \overline{U}$ and Σ_{SFR} (e.g., Hirashita & Chiang 2022; Chiang et al. 2023, J. Chastenet et al. 2024, in preparation). Another quantity that shows a moderate correlation is W_{CO}. α_{CO} is expected to anticorrelate with W_{CO} due to either external pressure or other dynamical effects (e.g., Bolatto et al. 2013; Sun et al. 2018). The power-law index for W_{CO} is within the previously reported range of −0.32 to −0.54 (Narayanan et al. 2012; Gong et al. 2020; Hunt et al. 2023).

Compared to $\alpha_{CO\,(2-1)}$, the correlations between $\alpha_{CO\,(1-0)}$ and local conditions are overall weaker. log rsSFR has the strongest correlation with $\alpha_{CO\,(1-0)}$ in all three R_{21} cases, and $\log \overline{U}$ is the second strongest.

For all combinations of α_{CO} and local conditions, we perform linear regression with the functional form:

$$\log \alpha_{CO} = mx + b, \quad (16)$$

where x[23] is the local condition and both m and b are free parameters, all of which are listed in Table 3. In the same table, we also report the rms error (Δ_{rms}) between the measured and fitted $\log \alpha_{CO}$. Most formulae have $\Delta_{rms} \sim 0.2$ dex. W_{CO}, $\overline{U}$,

[22] The regression for most quantities is done on a logarithmic scale. See Table 3.
[23] Note that most x quantities are in logarithmic scale.

Table 3
Correlation and Linear Regression between Pixel-by-pixel α_{CO} Measurements and Local Physical Quantities

$\log \alpha_{CO\,(2-1)}$, CO (2–1) Only					
$x^{(1)}$	ρ	$m^{(1)}$	$b^{(1)}$	Δ_{rms}	$\rho_{norm}^{(2)}$
$\log W_{CO}$	−0.67	−0.49 ± 0.01	1.01 ± 0.0	0.17	−0.33
12 + log(O/H)	−0.48	−2.62 ± 0.06	23.2 ± 0.5	0.22	−0.2
$\log \Sigma_{dust}$	−0.44	−0.66 ± 0.01	0.15 ± 0.01	0.24	−0.29
$\log \overline{U}$	−0.73	−0.97 ± 0.01	1.15 ± 0.0	0.19	−0.4
$\log \Sigma_\star$	−0.32	−0.38 ± 0.01	1.57 ± 0.02	0.23	−0.4
$\log \Sigma_{SFR}$	−0.59	−0.48 ± 0.01	−0.18 ± 0.01	0.17	−0.3
log sSFR	−0.22	−0.12 ± 0.01	−0.4 ± 0.1	0.27	0.1
R_g/R_{25}	0.43	0.8 ± 0.02	0.56 ± 0.01	0.23	0.38

$\log \alpha_{CO\,(1-0)}$, CO (1–0) Only					
x	ρ	m	b	Δ_{rms}	$\rho_{norm}^{(2)}$
$\log W_{CO}$	−0.42	−0.39 ± 0.01	0.83 ± 0.01	0.18	−0.43
12 + log(O/H)	−0.32	−1.81 ± 0.08	16.0 ± 0.7	0.2	−0.17
$\log \Sigma_{dust}$	−0.07	−0.14 ± 0.02	0.39 ± 0.02	0.21	−0.22
$\log \overline{U}$	−0.35	−0.71 ± 0.02	0.8 ± 0.01	0.19	−0.23
$\log \Sigma_\star$	−0.04	−0.12 ± 0.01	0.76 ± 0.02	0.23	−0.3
$\log \Sigma_{SFR}$	−0.31	−0.29 ± 0.01	−0.05 ± 0.02	0.19	−0.24
log sSFR	−0.26	−0.22 ± 0.02	−1.7 ± 0.2	0.22	0.1
R_g/R_{25}	0.25	0.56 ± 0.03	0.36 ± 0.01	0.21	0.29

$\log \alpha_{CO\,(1-0)}$, $w/R_{21}(I_{W4})$					
x	ρ	m	b	Δ_{rms}	$\rho_{norm}^{(2)}$
$\log W_{CO}$	−0.46	−0.41 ± 0.01	0.84 ± 0.01	0.18	−0.29
12 + log(O/H)	−0.4	−2.19 ± 0.07	19.3 ± 0.6	0.21	−0.19
$\log \Sigma_{dust}$	−0.17	−0.25 ± 0.02	0.31 ± 0.02	0.22	−0.17
$\log \overline{U}$	−0.34	−0.7 ± 0.02	0.8 ± 0.01	0.19	−0.19
$\log \Sigma_\star$	−0.15	−0.18 ± 0.01	0.92 ± 0.02	0.23	−0.3
$\log \Sigma_{SFR}$	−0.31	−0.31 ± 0.01	−0.07 ± 0.02	0.19	−0.22
log sSFR	−0.2	−0.08 ± 0.01	−0.3 ± 0.1	0.24	0.16
R_g/R_{25}	0.31	0.64 ± 0.03	0.36 ± 0.01	0.21	0.28

$\log \alpha_{CO\,(1-0)}$, $w/R_{21} = 0.65$					
x	ρ	m	b	Δ_{rms}	$\rho_{norm}^{(2)}$
$\log W_{CO}$	−0.45	−0.4 ± 0.01	0.84 ± 0.01	0.18	−0.28
12 + log(O/H)	−0.4	−2.29 ± 0.08	20.1 ± 0.7	0.22	−0.18
$\log \Sigma_{dust}$	−0.16	−0.25 ± 0.02	0.31 ± 0.02	0.22	−0.15
$\log \overline{U}$	−0.37	−0.73 ± 0.02	0.82 ± 0.01	0.19	−0.2
$\log \Sigma_\star$	−0.16	−0.19 ± 0.01	0.95 ± 0.02	0.24	−0.3
$\log \Sigma_{SFR}$	−0.32	−0.3 ± 0.01	−0.07 ± 0.02	0.19	−0.22
log sSFR	−0.26	−0.14 ± 0.01	−0.8 ± 0.1	0.26	0.15
R_g/R_{25}	0.32	0.68 ± 0.03	0.35 ± 0.01	0.22	0.28

Note. All correlation coefficients presented have their p-values smaller than 0.05. (1) The linear regression formula is $\log \alpha_{CO} = mx + b$. An uncertainty of ±0.0 represents that the rounded uncertainty in the parameter is smaller than 0.01. (2) Correlation coefficients calculated with α_{CO} normalized by W_{CO}-weighted mean value in each galaxy. We underline the cases where the correlation of normalized α_{CO} is stronger than the one without normalization.

and Σ_{SFR} have the strongest correlations and smallest Δ_{rms} in general.

One quantity that is often used for parameterizing α_{CO} is 12 + log(O/H). In our measurements, α_{CO} has a moderate to weak correlation with 12 + log(O/H) in all cases. The slope from linear regression (m) is −2.6 for $\alpha_{CO\,(2-1)}$ and −1.8 to −2.3 for $\alpha_{CO\,(1-0)}$. These values are mildly steeper than most literature values (∼ −1.6 to −2.0, Bolatto et al. 2013; Hunt et al. 2015; Accurso et al. 2017; Sun et al. 2020), but are still within the previously reported range, e.g., −2.0 to −2.8 in Schruba et al. (2012). Note that our data set is less suitable for an in-depth study on 12 + log(O/H) as >80% of our data are concentrated in a small dynamic range of $8.4 \leqslant 12 + \log(O/H) \leqslant 8.6$.

We also calculate the correlation between physical quantities and normalized α_{CO}. In this calculation, α_{CO} is normalized by the W_{CO}-weighted mean in each galaxy. For most quantities, the correlation becomes weaker after normalization. Meanwhile, $\Sigma_\star$ has a stronger correlation with normalized α_{CO} in all

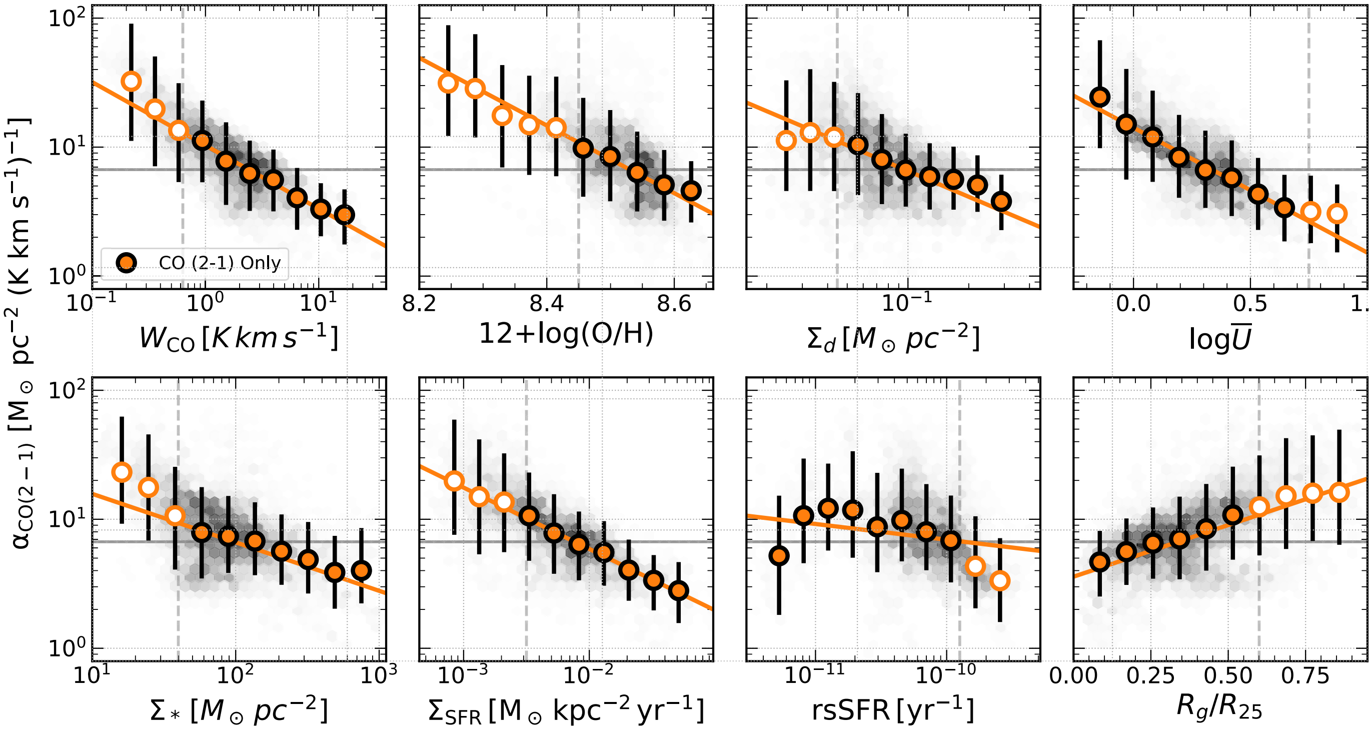

Figure 3. Our measured $\alpha_{CO\,(2-1)}$, measured with $W_{CO\,(2-1)}$ data only, as a function of the environmental parameters. The orange circles show the median of binned data. The error bars include both the scatter within a bin and uncertainties in pixel-by-pixel measurements. The orange line shows the linear regression between $\alpha_{CO\,(2-1)}$ and the quantity on the horizontal axis. The empty circles indicate bins where the quantity in the horizontal axis is incomplete, i.e., less than 50% of the pixels have S/N >1 in W_{CO} and Herschel bands (see Section 3.3). The dashed vertical line shows the 50% boundary. The gray-shaded region shows the hexagonal-binned pixel-by-pixel measurements. The gray horizontal line shows the value of α_{CO}^{MW}, converted to $\alpha_{CO\,(2-1)}$ assuming $R_{21} = 0.65$.

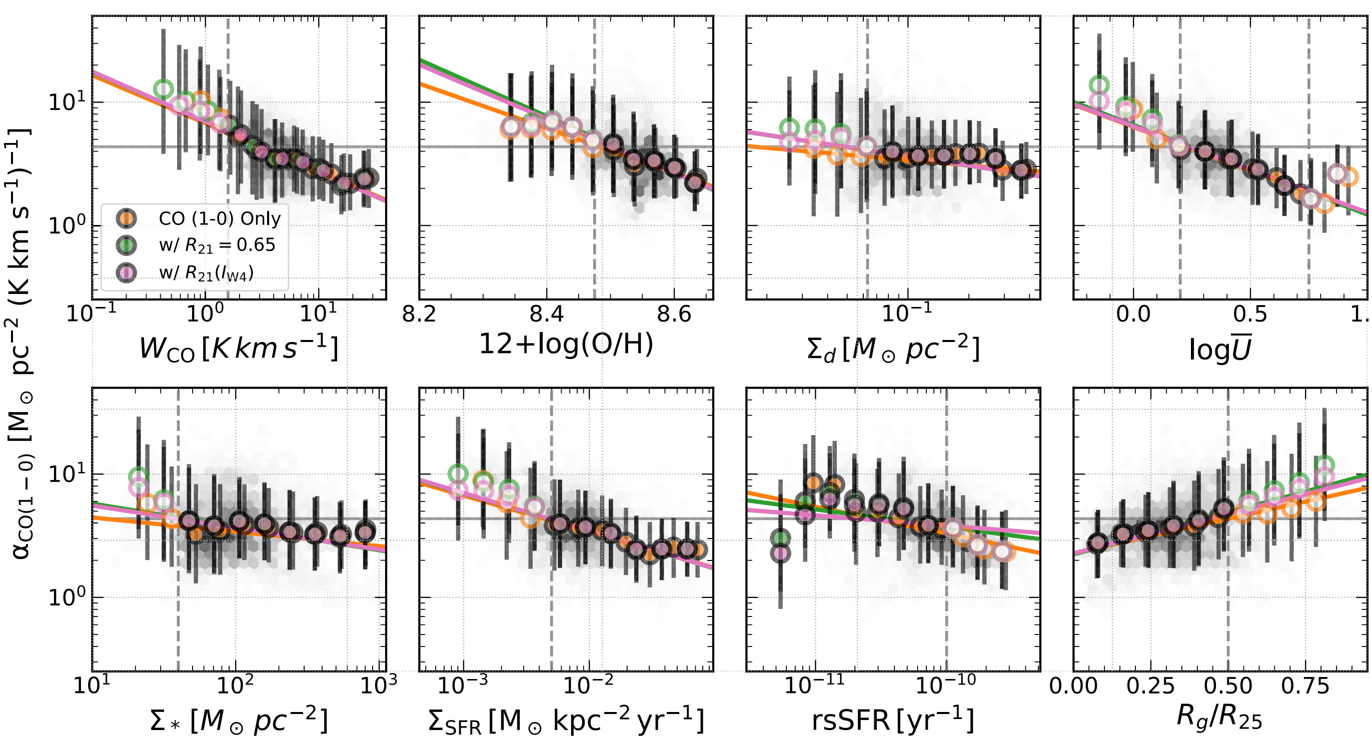

Figure 4. Similar to Figure 3, but for $\alpha_{CO\,(1-0)}$ measurements. The three colors of the circles and lines show the three cases indicated in the legend. CO (1–0) Only: measured with $W_{CO\,(1-0)}$ data only; $w/R_{21} = 0.65$ and $w/R_{21}(I_{W4})$: measured with $W_{CO\,(1-0)}$ and $W_{CO\,(2-1)}$ data for galaxies without $W_{CO\,(1-0)}$. The background graded region is plotted for the "CO (1–0) Only" measurements.

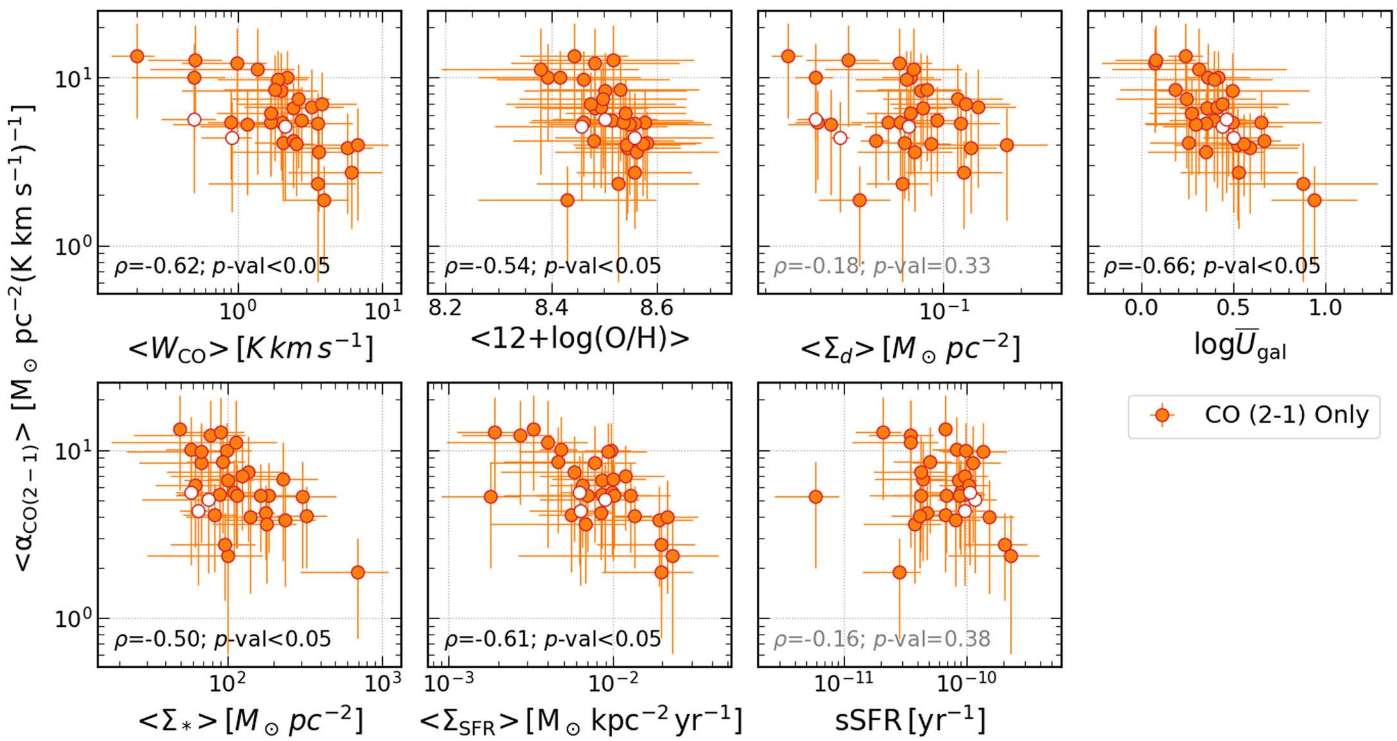

Figure 5. Scaling relations between galaxy-averaged $\alpha_{\rm CO\,(2-1)}$ and environmental parameters. The error bars show the 16th–84th percentiles in each galaxy. All data points are calculated with $W_{\rm CO\,(2-1)}$ data only. The filled markers show the galaxies with $W_{\rm CO}$ recovery fraction $\geqslant$50%, while the empty markers show the <50% ones (Table 2). The correlation coefficients and *p*-values are labeled at the lower left in each panel, highlighting the significant (*p*-value <0.05) ones. We use weighted averaged for $\alpha_{\rm CO}$, $\overline{U}$ and sSFR, and simple averages for the other quantities. Please see Section 4.2 for details.

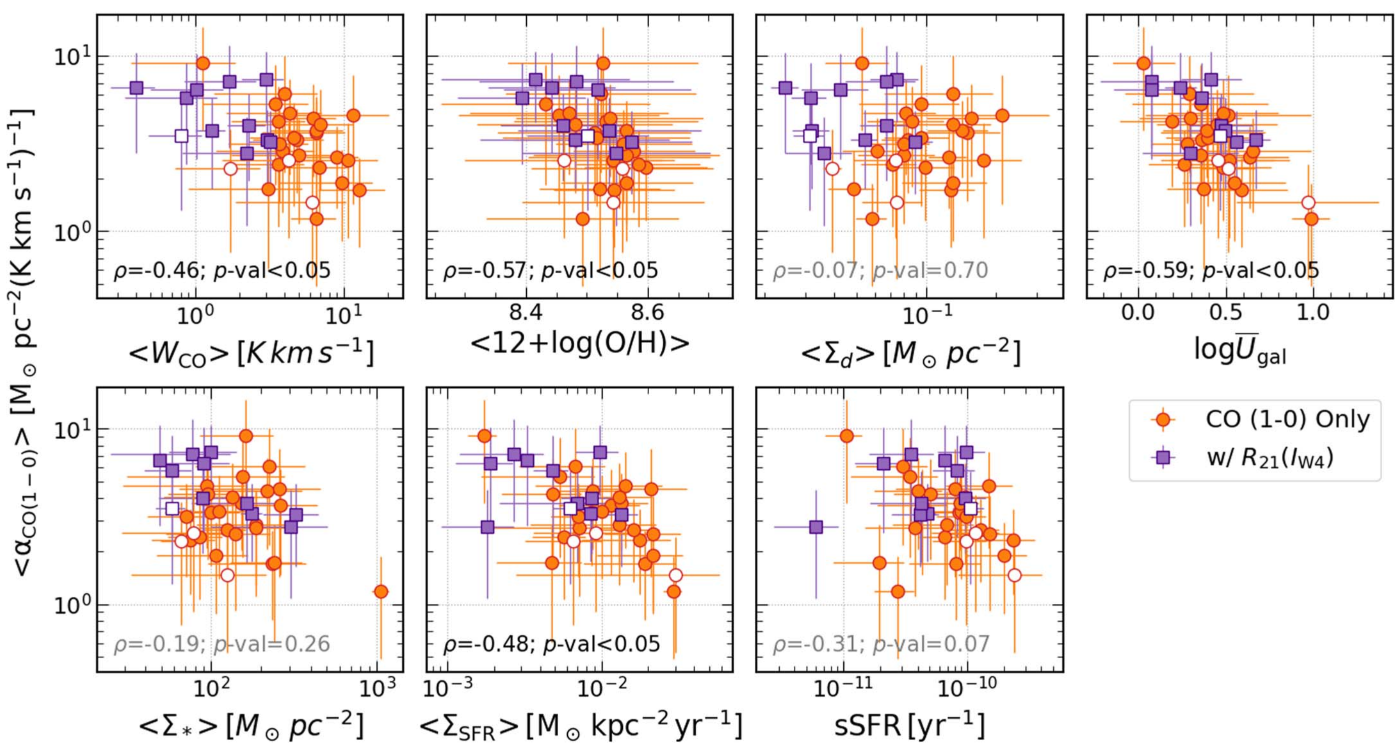

Figure 6. Similar to Figure 5 but for $\alpha_{\rm CO\,(1-0)}$ measurements. The orange points show the measurements with $W_{\rm CO\,(1-0)}$ data only, and the purple points show measurements with $W_{\rm CO\,(2-1)}$ data with an $I_{\rm W4}$-dependent R_{21}. The fixed R_{21} results are similar to the ones from $I_{\rm W4}$-dependent R_{21}. They are not displayed for clarity.

cases in Table 3, indicating that $\Sigma_\star$ traces the intragalaxy $\alpha_{\rm CO}$ variations after normalization of galaxy-to-galaxy differences.

Overall, we have shown that $\alpha_{\rm CO\,(2-1)}$ has stronger correlations with local conditions than $\alpha_{\rm CO\,(1-0)}$. Among the local quantities, $W_{\rm CO}$, $\overline{U}$, and $\Sigma_{\rm SFR}$ usually have stronger correlations with $\alpha_{\rm CO}$. We do not see a strong correlation coefficient between $\alpha_{\rm CO}$ and 12 + log(O/H), one of the most frequently used quantities to model $\alpha_{\rm CO}$.

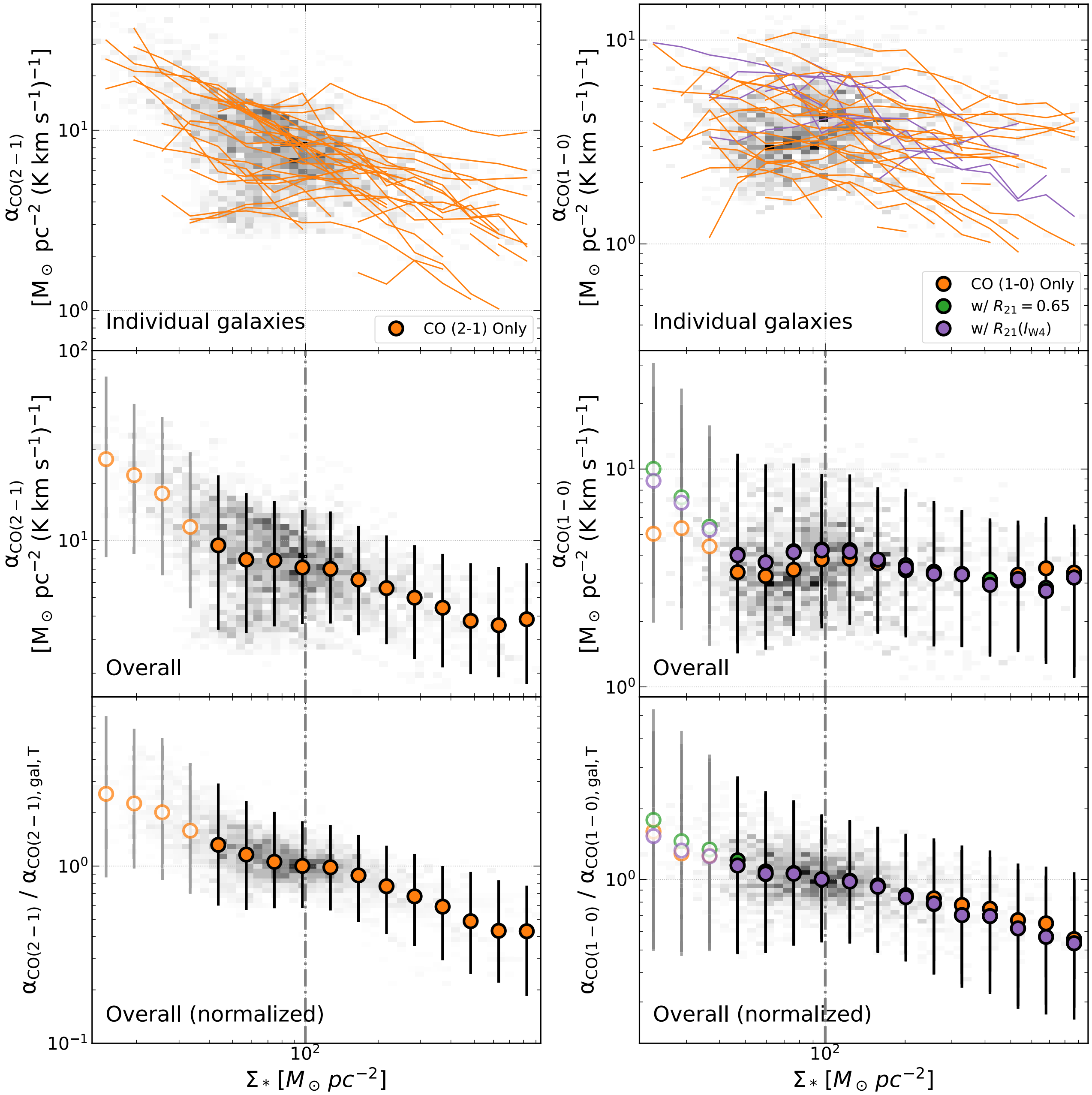

Figure 7. Measured α_{CO} plotted against stellar mass surface density. The left panels show the $\alpha_{CO\,(2-1)}$ measurements while the right panels show the $\alpha_{CO\,(1-0)}$ measurements. Top panels: the measured α_{CO} in each galaxy, where the solid lines show the median in each $\Sigma_\star$ bin. Middle panels: the overall binned median of α_{CO}, where the error bars show the 16th and 84th percentiles. Bottom panels: similar to the middle panels, but the *y*-axis is normalized to the α_{CO} value at $\Sigma_{\star,T} = 100\ M_\odot pc^{-2}$ (shown in vertical dashed line) in each galaxy. The galaxies with α_{CO} increasing with $\Sigma_\star$ are removed in the bottom panels. The 2d histogram in all panels shows the overall data distribution.

4.2. Correlation with Galaxy-averaged Quantities

Besides kpc-scale variations, we also test how galaxy-averaged $\alpha_{CO\,(2-1)}$ and $\alpha_{CO\,(1-0)}$ vary between galaxies, and how their variations correlate with galaxy-averaged properties. The results are visualized in Figures 5–6. We use the symbol $<X>$ to represent the simple averaged value of quantity X in each galaxy, i.e., $\Sigma_i^{gal} X_i / \Sigma_i^{gal}$, where Σ_i^{gal} is the summation over all pixels in a galaxy. There are three quantities for which we do not apply simple averages: (1) as mentioned in Section 4, we will present the W_{CO}-weighted mean of α_{CO}; (2) $\log \overline{U}_{gal}$ is calculated as $\log(\Sigma_i^{gal} \Sigma_{dust,i} \overline{U}_i / \Sigma_i^{gal} \Sigma_{dust,i})$ to reflect the dust-mass-weighted averaged ISRF; (3) sSFR is calculated as $\Sigma_i^{gal} \Sigma_{SFR,i} / \Sigma_i^{gal} \Sigma_{\star,i} = SFR/M_\star$. The error bars in Figures 5– 6 show the 16th–84th percentiles of the corresponding quantity. In Figure 6, we also include $\alpha_{CO\,(1-0)}$ calculated with CO (2–1) data with an I_{W4}-dependent R_{21}. We only include one R_{21} prescription here for clarity.

We report the correlation coefficients and the corresponding *p*-values in each panel of Figures 5–6. Compared to the results in Section 4.1, we note that whether a quantity has a significant correlation with α_{CO} and the strength of the correlation often differ between the spatially resolved case and the galaxy-averaged case. Several quantities show significant correlations with $<\alpha_{CO}>$. $12 + \log(O/H)$ and $<\Sigma_{SFR}>$seem to show stronger correlation with $<\alpha_{CO}>$for both CO (2–1) and

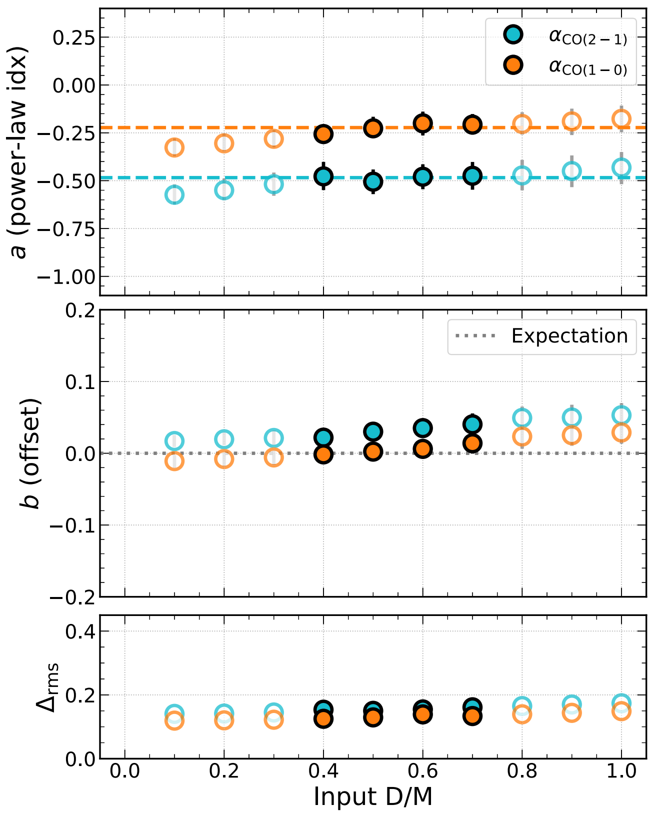

Figure 8. Dependence of fitted power-law index and offset on assumed D/M. The cyan points show results for $\alpha_{CO\,(2-1)}$, and the orange points show results for $\alpha_{CO\,(1-0)}$. For $\alpha_{CO\,(1-0)}$, we only show results from $W_{CO\,(1-0)}$ data only as the fitting results, including $W_{CO\,(2-1)}$ data, have a minimal difference. We highlight the region with D/M inferred from literature, i.e., $0.4 \leqslant D/M \leqslant 0.7$, while the empty circles show results outside that range. Top: power-law index (a). The dashed lines show the mean value of a in the range of $0.4 \leqslant D/M \leqslant 0.7$. Middle: offset ($b$). The dotted line shows $b = 0$, where expect the fitting result to be if α_{CO} monotonically decreases with $\Sigma_\star$. Bottom: Δ_{rms} of each fit.

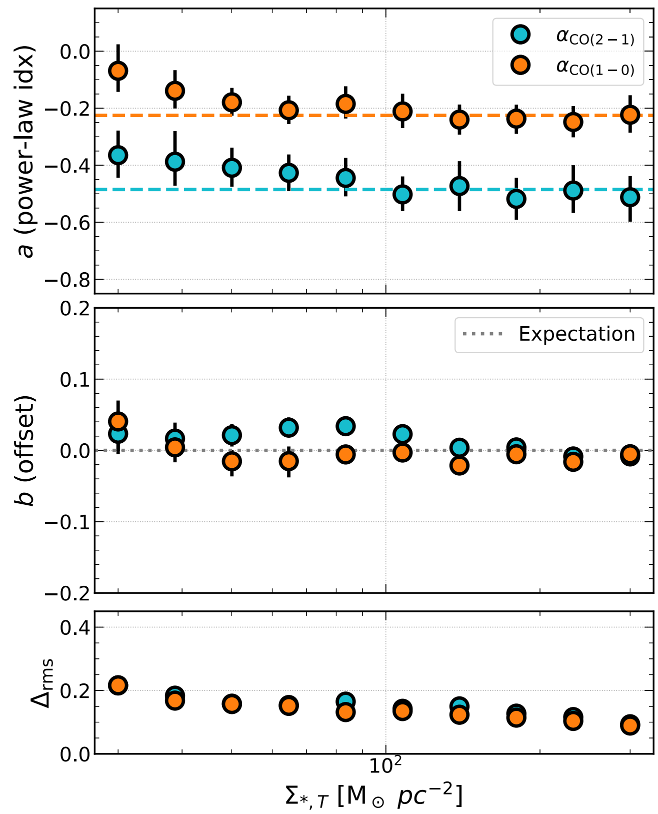

Figure 9. Dependence of fitted power-law index and offset on adopted threshold $\Sigma_{\star,T}$. The cyan points show results for $\alpha_{CO\,(2-1)}$, and the orange points show results for $\alpha_{CO\,(1-0)}$. For $\alpha_{CO\,(1-0)}$, we only show results from $W_{CO\,(1-0)}$ data only as the fitting results, including $W_{CO\,(2-1)}$ data, have a minimal difference. Top: power-law index (a). The dashed lines show the average a values with $\Sigma_{\star,T} = 100\,M_\odot pc^{-2}$ in the range of $0.4 \leqslant D/M \leqslant 0.7$. These are the same lines as Figure 8. Middle: offset (b). The dotted line shows $b = 0$, where expect the fitting result to be if α_{CO} monotonically decreases with $\Sigma_\star$. Bottom: Δ_{rms} of each fit. All the calculations here are done with $D/M = 0.55$.

CO (1–0) than in the spatially resolved case. The insignificant correlation between $<\Sigma_\star>$ and $\alpha_{CO\,(1-0)}$ is consistent with the findings of Carleton et al. (2017) and Dunne et al. (2022), assuming that $\Sigma_\star$ dominates the total mass surface density and that CO (1–0) dominates the CO measurements.

5. Power-law Dependence of the Conversion Factor on Stellar Mass Surface Density

In the α_{CO} prescription proposed in Bolatto et al. (2013), the authors use a power law with Σ_{Total} ($=\Sigma_\star + \Sigma_{gas}$) to trace the changes in α_{CO} due to CO emissivity variations (related to gas temperature and opacity) and a threshold in Σ_{Total} to trace where the effects become important. Inspired by their work and motivated by the necessity of improving α_{CO} prescriptions in galaxy centers, we examine whether a similar functional form applies to our α_{CO} measurements. Furthermore, as shown in the previous section, the correlation between $\Sigma_\star$ and α_{CO} improves after normalizing α_{CO} the W_{CO}-weighted mean, which could fit into the picture of separating CO-dark and starburst components in Bolatto et al. (2013). With the WISE full-sky observations, the resolved $\Sigma_\star$ for all nearby galaxies is widely available, which makes this kind of prescription easy to apply. In this study, we will focus on the α_{CO}-to-$\Sigma_\star$ relation instead of Σ_{Total} because our data set is mostly $\Sigma_\star$-dominated (50% with $\Sigma_{gas}/\Sigma_{Total} < 0.2$; 99.5% with $\Sigma_{gas}/\Sigma_{Total} < 0.5$).

We present the correlations between α_{CO} and $\Sigma_\star$ in Figure 7 for both $\alpha_{CO\,(2-1)}$ (left panels) and $\alpha_{CO\,(1-0)}$ (right panels). In the top panels, we present the profile of measured α_{CO} versus $\Sigma_\star$ in each galaxy. For $\alpha_{CO\,(2-1)}$, most galaxies have their α_{CO} anticorrelate with $\Sigma_\star$ at $\Sigma_\star > 100\,M_\odot pc^{-2}$ aside from a few exceptions. It is similar for $\alpha_{CO\,(1-0)}$ but with a flatter α_{CO}-to-$\Sigma_\star$ slope. At the low-$\Sigma_\star$ end, some galaxies still have negative α_{CO}-to-$\Sigma_\star$ correlations while others have strong positive correlations. In the middle panels, we show the collective behavior across galaxies using a binned average as a function of $\Sigma_\star$, with each bin spanning ~0.1 dex in $\Sigma_\star$.

We find that in regions with high $\Sigma_\star$, α_{CO} generally decreases with $\Sigma_\star$, which is consistent with the negative power-law index in the Bolatto et al. (2013) formula. There appears to be galaxy-to-galaxy variation in the value of α_{CO}, but good agreement in the rate of how fast α_{CO} decreases with $\Sigma_\star$. To better illustrate this phenomenon, we normalize α_{CO} in each galaxy at a threshold $\Sigma_{\star,T} \equiv 100\,M_\odot pc^{-2}$ (a threshold inspired by Bolatto et al. 2013) and show the normalized α_{CO} in the bottom panel of Figure 7. The normalization in each galaxy ($\alpha_{CO,gal,T}$) is defined as the median α_{CO} of pixels with their $\Sigma_\star$ within $\Sigma_{\star,T} \pm 0.05$ dex.

In the remainder of this section, we will focus on analyzing the scaling relation between α_{CO} and $\Sigma_\star$ in a subsample of galaxies with at least five measurements with $\Sigma_\star > \Sigma_{\star,T}$ (29 galaxies

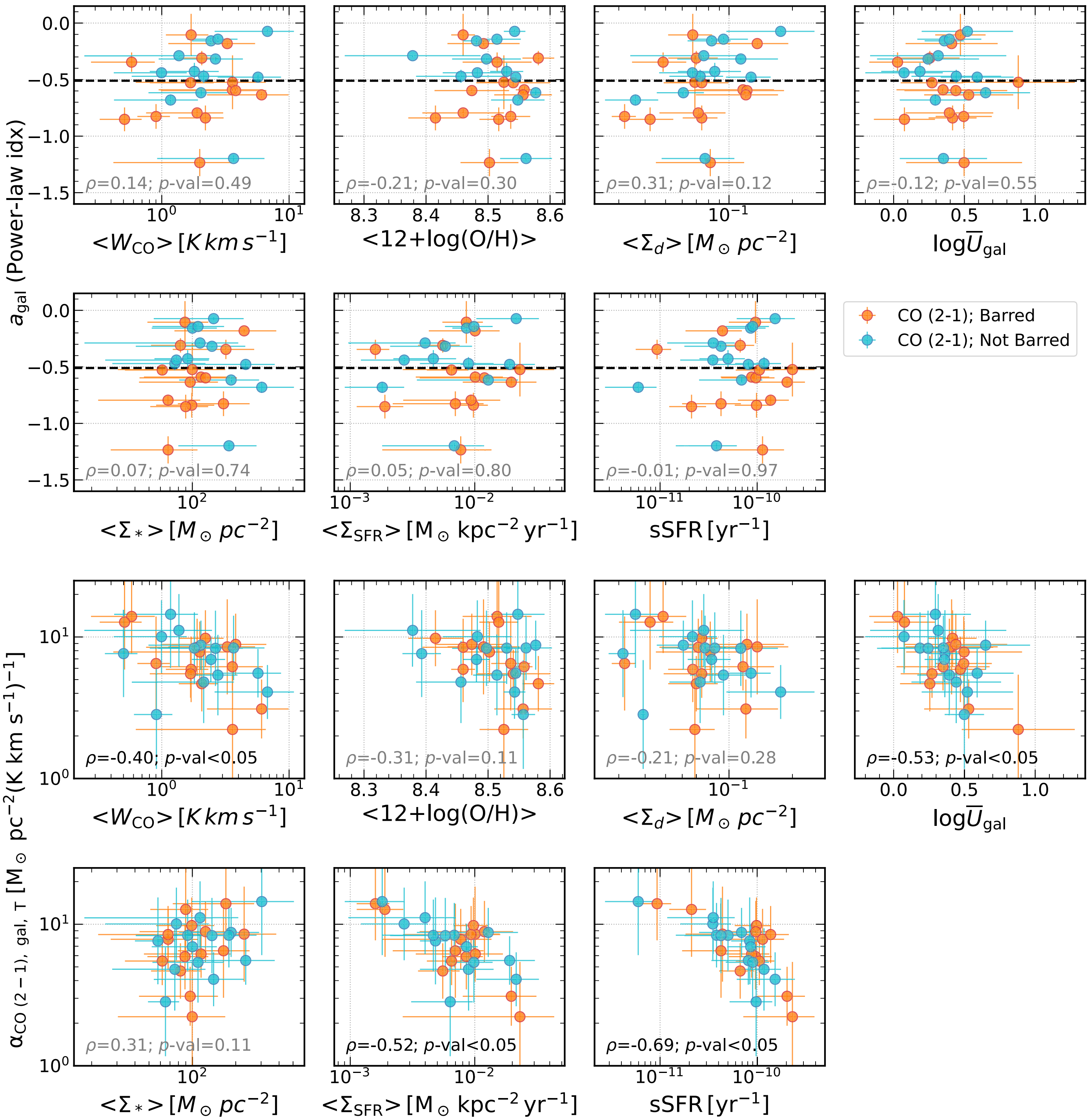

Figure 10. Scaling relations between $a_{\rm gal}$ (the power-law index), $\alpha_{\rm CO,gal,T}$, and galaxy-averaged environmental parameters for CO (2–1) data. Galaxies that are barred and not barred are colored orange and cyan, respectively. The black dashed line in $a_{\rm gal}$ shows the a value calculated from the overall data. The correlation coefficients and p-values are labeled at the lower left in each panel, highlighting the significant (p-value <0.05) ones.

for CO (2–1) and 25 galaxies for CO (1–0); see the $N_{pix,100}$ column in Table 2). We use a power law to characterize this scaling relation:

$$\log \frac{\alpha_{\rm CO}}{\alpha_{\rm CO,gal,T}} = a \times \log \frac{\Sigma_\star}{\Sigma_{\star,\rm T}} + b,\ \ \Sigma_\star \geqslant \Sigma_{\star,\rm T}, \quad (17)$$

where a (the power-law index) and b (the offset) are free parameters. As both $\alpha_{\rm CO}$ and $\Sigma_\star$ are normalized in the formula, we expect $b \sim 0$ (and $b_{\rm gal} \sim 0$) if $\alpha_{\rm CO}$ monotonically decreases with $\Sigma_\star$. By default, we fit Equation (17) with all data. When fitting data in individual galaxies only, we will describe the parameters as $a_{\rm gal}$ and $b_{\rm gal}$.

We exclude data from galaxies that do not satisfy the following criteria: (1) at least five measurements at $\Sigma_\star > \Sigma_{\star,\rm T}$; (2) spanning at least 0.1 dex in $\Sigma_\star$ at $\Sigma_\star > \Sigma_{\star,\rm T}$. As all criteria are $\Sigma_{\star,\rm T}$-dependent, we expect the size of the subsample space to vary with $\Sigma_{\star,\rm T}$. We will visualize the galaxies not satisfying the last two criteria in Section 5.2.

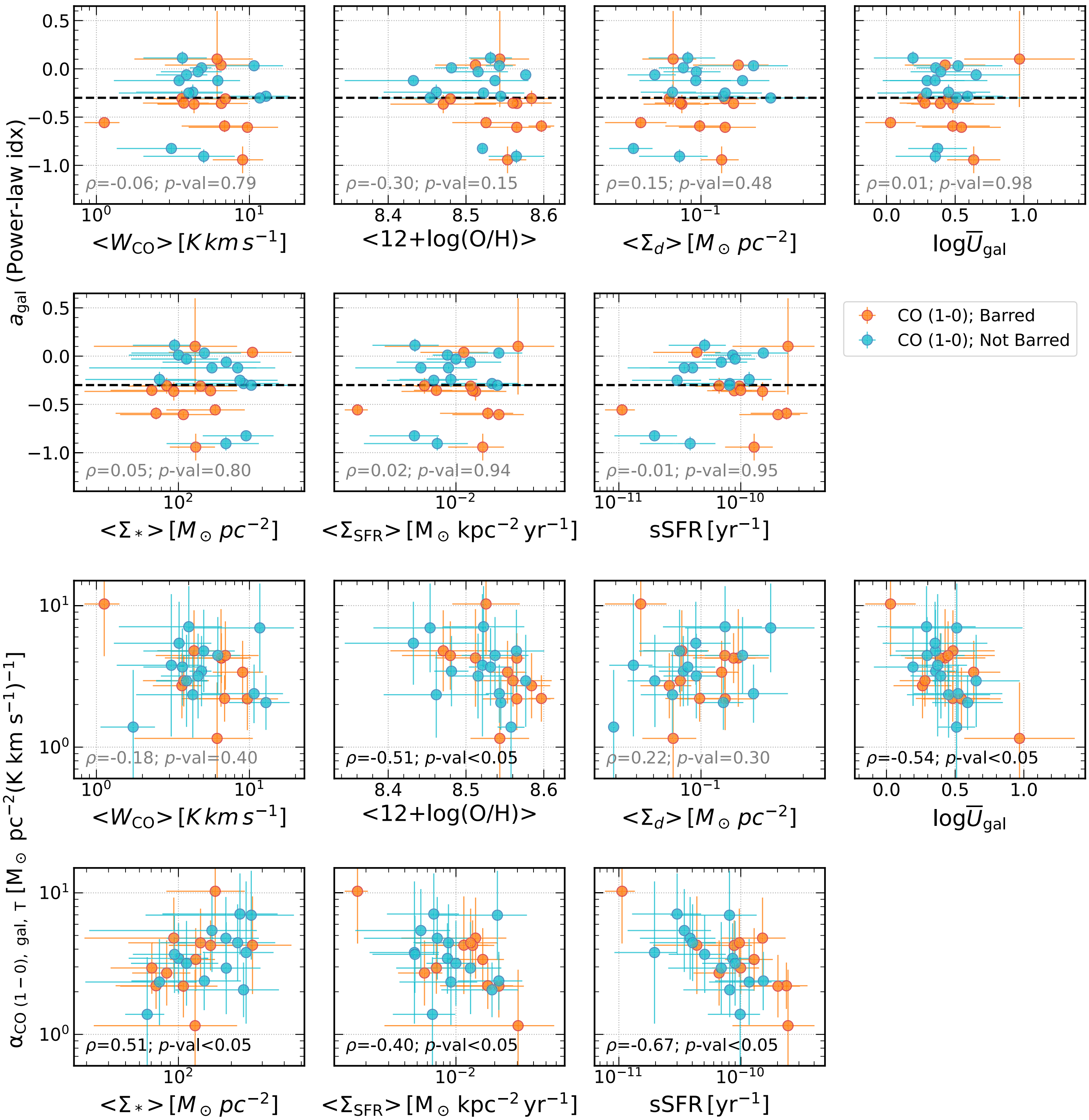

Figure 11. Similar to Figure 10, but for CO (1–0) data.

With the fiducial setting, i.e., D/M = 0.55 and $\Sigma_{\star,\rm T} = 100\,M_\odot{\rm pc}^{-2}$, the fitting yields $a = -0.50^{+0.07}_{-0.06}$ and $b = 0.03^{+0.01}_{-0.01}$ with $\Delta_{\rm rms} = 0.15$ dex for CO (2–1); $a = -0.22^{+0.06}_{-0.06}$ and $b = 0.003^{+0.01}_{-0.01}$ with $\Delta_{\rm rms} = 0.13$ dex for CO (1–0).[24] The small b values, which are consistent with our expectations, indicate that the $\alpha_{\rm CO}$-to-$\Sigma_\star$ relation matches with the picture of a simple power law. The difference between a values for CO (2–1) and CO (1–0) data is consistent with the finding that $R_{21} \propto I_{\rm MIR}^{-0.2}$ (Leroy et al. 2023). The uncertainties in a and b are estimated from 1000 rounds of bootstrap resampling. In each round, we select 29 (25) galaxies for CO (2–1) (CO (1–0)) data with replacement from our sample galaxies to fit the power law. We then take the difference between the best-fit parameter and the 84$^{\rm th}$ (16$^{\rm th}$) percentile from the 1000 bootstraps as the upper (lower) uncertainty.

[24] A recent review (E. Schinnerer & A. K. Leroy ARA&A submitted) indicates a slightly different result of $a \sim -0.25$ for $\alpha_{\rm CO\,(1-0)}$, which is consistent with our result. The two main differences between this work and theirs are: (1) The Schinnerer & Leroy review adopts a different formula for $\Sigma_{\rm SFR}$-dependent R_{21}; (2) The Schinnerer & Leroy review combines all available CO (2–1) and CO (1–0) data, while we keep them separate in this section.

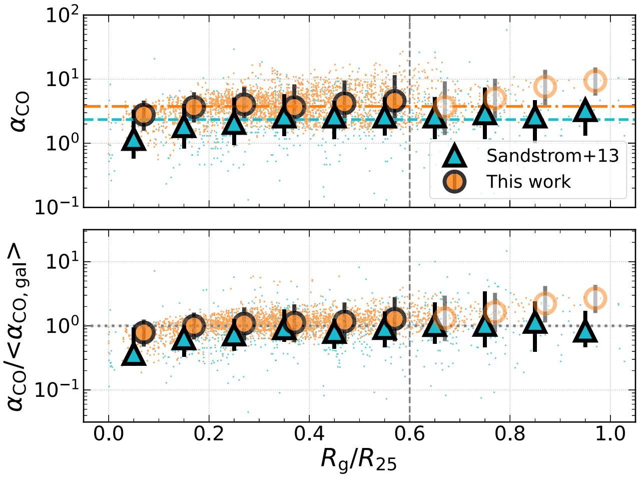

Figure 12. Relation between measured α_{CO} and galactocentric radius in this work and Sandstrom et al. (2013). For both works, we display $\alpha_{CO} = 0.65\alpha_{CO\,(2-1)}$ for uniformity. We only include measurements from the galaxies that are included in both works. The vertical dashed line shows the completeness threshold in R_g/R_{25} in this work. In the top panel, the horizontal cyan dashed-dotted line shows the mean α_{CO} in Sandstrom et al. (2013), and the orange dashed line shows the mean α_{CO} from this work. The two lines are close to each other. In the bottom panel, the horizontal line shows $\alpha_{CO} = <\alpha_{CO,gal}>$, where $<\alpha_{CO,gal}>$is the mean α_{CO} in each galaxy.

We will measure how the α_{CO}-to-$\Sigma_\star$ relation varies according to the adopted D/M and $\Sigma_{\star,T}$ in the remainder of this section. In the Appendix, we also test how the results would change with internal variations of D/M. Our toy model in the Appendix shows that *a* could be up to ∼0.2 steeper than the constant D/M case.

5.1. Dependence of the Power-law Index on Adopted D/M and $\Sigma_{\star,T}$

To test the robustness of our results for potentially different dust properties, we expand the assumed D/M from the single value (0.55) assumed in the previous section to the possible range of D/M, i.e., $0.1 \leqslant D/M \leqslant 1$. We do not go to even lower D/M values because our methodology relies on the existence of a certain amount of dust. We derive α_{CO} and fit the α_{CO}-to-$\Sigma_\star$ power-law relation at each assumed D/M. The results are shown in Figure 8. We highlight the fit results with $0.4 \leqslant D/M \leqslant 0.7$, which is the D/M value inferred from the literature introduced in Section 2. Same as in the previous calculations, the uncertainties in parameters *a* and *b* in the fitting parameters are estimated from 1000 rounds of bootstrap resampling.

As shown in the top panel of Figure 8, we find that the power-law index (*a*) is invariant with assumed D/M throughout the range we examine for both $\alpha_{CO\,(2-1)}$ and $\alpha_{CO\,(1-0)}$. The average *a* in the range of $0.4 \leqslant D/M \leqslant 0.7$ is $-0.48^{+0.08}_{-0.09}$ and $-0.22^{+0.08}_{-0.09}$ for $\alpha_{CO\,(2-1)}$ and $\alpha_{CO\,(1-0)}$, respectively. The statistical uncertainties in *a* for both CO transitions are around ±0.1 dex. The result implies that as long as the D/M stays roughly constant within each galaxy, we can recover similar behavior in the $\Sigma_\star$ dependence of α_{CO} with a power law.

Due to the nature of the definition of *b* in Equation (17), we expect $b \sim 0$. This is seen in most D/M values we examine as $|b|$ stays below 0.03, shown in the middle panel of Figure 8. This indicates that the power-law parameterization reasonably

Table 4
Dependence of $\alpha_{CO,gal,T}$ on Galaxy-integrated Quantities

$x^{(1)}$	$m^{(1)}$	$d^{(1)}$	Δ_{rms}
$\log \alpha_{CO\,(2-1),gal,T}$, CO (2–1) Only			
$<W_{CO}>$	-0.4 ± 0.1	1.0 ± 0.1	0.15
$\overline{U}_{gal}$	-0.4 ± 0.2	1.0 ± 0.1	0.16
$<\Sigma_{SFR}>$	-0.4 ± 0.1	0.0 ± 0.2	0.13
sSFR	-0.5 ± 0.1	-3.9 ± 0.9	0.11
$\log \alpha_{CO\,(1-0),gal,T}$, CO (1–0) Only			
x	m	d	Δ_{rms}
<12+log(O/H)>	-2.0 ± 0.9	17.8 ± 7.4	0.17
$\overline{U}_{gal}$	-0.7 ± 0.3	0.8 ± 0.1	0.16
$<\Sigma_\star>$	0.5 ± 0.2	-0.4 ± 0.4	0.17
$<\Sigma_{SFR}>$	-0.4 ± 0.2	-0.2 ± 0.3	0.16
sSFR	-0.4 ± 0.1	-3.9 ± 1.0	0.13

Note. (1) The linear regression formula is $\log \alpha_{CO,gal,T} = m \log x + d$ for most quantities and $\log \alpha_{CO,gal,T} = mx + d$ for <12+log(O/H)>. W_{CO} in [K km s^{-1}], Σ_{SFR} in [$M_\odot$ yr^{-1} kpc^{-2}], $\Sigma_\star$ in [$M_\odot$pc^{-2}] and sSFR in [yr^{-1}].

fits the observed data regardless of the assumed D/M value. However, the *b* values for $\alpha_{CO\,(2-1)}$ seem biased toward the positive end. This could result from a steeper log α_{CO}-to-log $\Sigma_\star$ slope toward higher $\Sigma_\star$, which results in a positive offset in the power law at relatively lower $\Sigma_\star$. In the bottom panel, we show the Δ_{rms} value of each fit as an indicator of goodness of fit. All fits have Δ_{rms} below 0.2 dex, and the fits around $0.4 \leqslant D/M \leqslant 0.7$ have $\Delta_{rms} \sim 0.14$ dex.

We further test if the chosen threshold in stellar mass surface density, $\Sigma_{\star,T}$, will affect the fitting results. We fix D/M = 0.55 and fit the power-law relation at $\Sigma_{\star,T}$ ranges from 30 to 300 $M_\odot$pc^{-2}. Note that the number of galaxies included in the subsample changes in each case due to the threshold in $\Sigma_\star$. The results are shown in Figure 9.

In the top panel of Figure 9, we notice that the power-law index (*a*) has a larger dynamic range than the case where we alter D/M, but the index stays negative throughout the $\Sigma_{\star,T}$ range we examine. The power-law index for $\alpha_{CO\,(2-1)}$ stays within ±0.1 of the fiducial case, and the indices for $\alpha_{CO\,(1-0)}$ are consistent with the fiducial value at $\Sigma_{\star,T} > 60\,M_\odot$pc^{-2}. There is a weak trend that $|a|$ becomes larger toward larger $\Sigma_{\star,T}$. The small *b* values indicate that the power-law function form applies in general. We also show the Δ_{rms} values in the bottom panel. We have $\Delta_{rms} \leqslant 0.2$, with a weak trend of smaller Δ_{rms} toward higher $\Sigma_{\star,T}$.

To summarize, the power-law functional form applies to the normalized α_{CO}-to-$\Sigma_\star$ relation within the D/M and $\Sigma_{\star,T}$ ranges we examine. With a fixed $\Sigma_{\star,T}$ at 100 $M_\odot$pc^{-2}, we find an invariant power-law index (*a*) throughout $0.1 \leqslant D/M < 1.0$. The average *a* in the range of $0.4 \leqslant D/M \leqslant 0.7$ is $-0.48^{+0.08}_{-0.09}$ and $-0.22^{+0.08}_{-0.09}$ for $\alpha_{CO\,(2-1)}$ and $\alpha_{CO\,(1-0)}$, respectively. With a fixed D/M at 0.55, we find a weak trend of larger $|a|$ toward higher $\Sigma_{\star,T}$. The power-law index derived with the fiducial setup, i.e., D/M = 0.55 and $\Sigma_{\star,T} = 100\,M_\odot$pc^{-2}, is a good representative of conditions with $60 < \Sigma_{\star,T} \leqslant 300\,M_\odot$pc^{-2}, with a span $\sim \pm 0.09$.

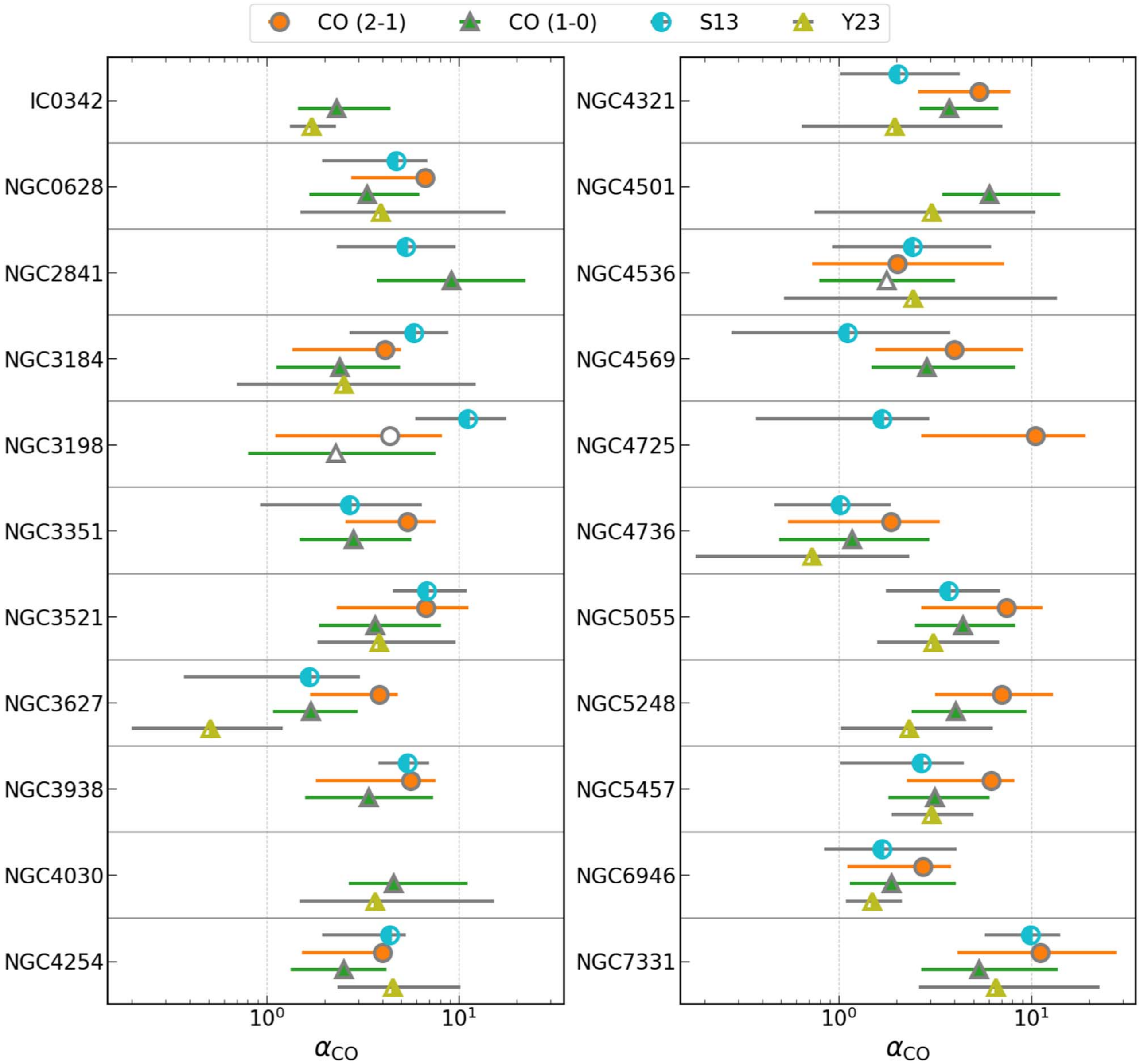

Figure 13. Mean α_{CO} values in each galaxy from this work (both CO (2–1) data with $R_{21} = 0.7$ and CO (1–0) data; Sandstrom et al. 2013, S13) and the COMING survey (Sorai et al. 2019; Yasuda et al. 2023, Y23). Circles show α_{CO} values derived with CO (2–1) data, and triangles show α_{CO} values derived with CO (1–0) data. Filled symbols show the results from this work, empty symbols show the ones with low CO recovery fraction (Table 2), and half-filled symbols show literature values. We only include galaxies that are measured in at least one of the literature surveys. The error bar for this work shows the 16th and 84th percentiles (Table 2). The mean and error bars of previous works are quoted from Table 4 of Sandstrom et al. (2013, with rescaling for R_{21}) and Table 3 of Yasuda et al. (2023). The mean values are W_{CO}-weighted mean for this work and Sandstrom et al. (2013), and the "global" result for Yasuda et al. (2023).

5.2. Galaxy-to-galaxy Variations

In this section, we examine the possible variation in α_{CO}-to-$\Sigma_\star$ relation between individual galaxies, mainly how the variation in $\alpha_{CO,gal,T}$ (normalization of α_{CO} at $\Sigma_{\star,T}$; see Section 5) and a_{gal} (power-law index; Equation (17)) correlate with galaxy-averaged properties. By understanding what sets a_{gal} and $\alpha_{CO,gal,T}$, we can build a prescription of α_{CO} considering the α_{CO}-to-$\Sigma_\star$ relation and galaxy-to-galaxy variations. The results are visualized in Figures 10 and 11.

In the upper panels of Figures 10 and 11, we show how the power-law index (a_{gal}) varies with seven selected galaxy-averaged properties and whether the galaxy is barred or not. The set of properties is the same as the ones in Figures 5 and 6. None of the properties show a significant correlation with a_{gal}. Meanwhile, the standard deviation of a_{gal} is 0.30 for both CO (2–1) and CO (1–0).

In the lower panels of Figures 10 and 11, we show how the normalization in each galaxy ($\alpha_{CO,gal,T}$) varies with galaxy-averaged properties. The standard deviation of $\alpha_{CO,gal,T}$ is 0.2 dex for both CO (2–1) and CO (1–0). For CO (2–1), $<W_{CO}>$, $\log \overline{U}_{gal}$, $<\Sigma_{SFR}>$, and sSFR show significant correlations with $\alpha_{CO,gal,T}$ with similar strength. For CO (1–0), $<12 + \log(O/H)>$, $\log \overline{U}_{gal}$, $<\Sigma_\star>$, $<\Sigma_{SFR}>$ and sSFR show significant correlations with $\alpha_{CO,gal,T}$ with similar strength. We use these significant correlations to fit empirical relations for $\alpha_{CO,gal,T}$ and summarize the results in Table 4. The fitted empirical relations do not differ significantly in terms of Δ_{rms}.

Meanwhile, the fit with $\overline{U}$ has the smallest[25] statistical uncertainties in the fitted parameters among the parameters for both CO (2–1) and CO (1–0). Besides $\overline{U}$, $<\Sigma_{\rm SFR}>$ also has small statistical uncertainties and is available for more galaxies.

6. Discussion

6.1. General Suggestions for αCO Prescriptions

In Section 4.1, we present how the measured $\alpha_{\rm CO}$ correlates with local physical quantities and provide linear regression for each quantity at a 2 kpc scale in Table 2. These measurements consider the statistical behavior of the overall sample. Among the quantities, $W_{\rm CO}$, $\overline{U}$, and $\Sigma_{\rm SFR}$ usually have the strongest correlations with $\alpha_{\rm CO}$ and the smallest $\Delta_{\rm rms}$ from linear regression. We would suggest the readers go with these parameters if the parameter space of their sample overlaps with this study (see Figure 1 for the completeness of each quantity).

Meanwhile, we explicitly explore the relation between $\alpha_{\rm CO}$ and $\Sigma_\star$ in Section 5 as a possible tracer for starburst $\alpha_{\rm CO}$ at a 2 kpc scale and find a strong correlation between $\alpha_{\rm CO}$ and $\Sigma_\star$ after normalization at some $\Sigma_\star$ threshold. There are two ways to adopt these results. The first one is a stand-alone prescription combining the indices from Section 5.1 and normalization from Table 4, using galaxy-averaged $\overline{U}_{\rm gal}$ as an example:

$$\alpha_{\rm CO\,(2-1)} = 10^{-0.4\log(\overline{U}_{\rm gal})+1.0}\left(\frac{\Sigma_\star}{\Sigma_{\star,\rm T}}\right)^{-0.48}, \quad \Sigma_\star \geqslant \Sigma_{\star,\rm T} = 100\,M_\odot\ {\rm pc}^{-2},\ \text{and} \tag{18}$$

$$\alpha_{\rm CO\,(1-0)} = 10^{-0.7\log(\overline{U}_{\rm gal})+0.8}\left(\frac{\Sigma_\star}{\Sigma_{\star,\rm T}}\right)^{-0.22}, \quad \Sigma_\star \geqslant \Sigma_{\star,\rm T} = 100\,M_\odot\ {\rm pc}^{-2}, \tag{19}$$

where $\alpha_{\rm CO}$ is in unit of $M_\odot\ {\rm pc}^{-2}({\rm K\ km\ s^{-1}})^{-1}$, and the $\overline{U}_{\rm gal}$-dependent normalization could be replaced with other quantities listed in Table 4, e.g., $<\Sigma_{\rm SFR}>$. Please refer to Section 5 for relevant uncertainties. We note that the possible variation in the power-law index could be up to ∼0.2 due to internal variations in D/M (Appendix).

On the other hand, one key mechanism that sets $\alpha_{\rm CO}$, the CO-dark gas, is likely not parameterized by our formula (see Section 6.2). This is because the CO-dark gas effect is relatively weak in the metallicity span of our sample. However, both the CO-dark gas and the "starburst $\alpha_{\rm CO}$" effects should be considered for an $\alpha_{\rm CO}$ prescription to be applied through all environments. Thus, another suggestion we have is to make a Bolatto et al. (2013)-style combination (also see E. Schinnerer & A. K. Leroy, ARA&A submitted) of our $\Sigma_\star$ power-law term with existing $\alpha_{\rm CO}$ prescriptions tracing the CO-dark gas effect, e.g., Wolfire et al. (2010), Narayanan et al. (2012), Schruba et al. (2012), Hunt et al. (2015), Accurso et al. (2017), or Sun et al. (2020). That is, assuming the adopted existing CO-dark prescription is $\alpha_{\rm CO}^{\rm CO-dark}$, we suggest:

$$\alpha_{\rm CO\,(2-1)} = \begin{cases} \alpha_{\rm CO}^{\rm CO-dark}, & \Sigma_\star < \Sigma_{\star,\rm T} \\ \alpha_{\rm CO}^{\rm CO-dark}\left(\dfrac{\Sigma_\star}{\Sigma_{\star,\rm T}}\right)^{-0.48}, & \Sigma_\star \geqslant \Sigma_{\star,\rm T} \end{cases}. \tag{20}$$

Under this functional form, we expect the normalization ($\alpha_{\rm CO,gal,T}$) to be taken into account by the $\alpha_{\rm CO}^{\rm CO-dark}$ term. As this formula does not include our own normalization derived at $\Sigma_{\star,\rm T} = 100\,M_\odot{\rm pc}^{-2}$, one can adopt $60 \leqslant \Sigma_{\star,\rm T} \leqslant 300\,M_\odot{\rm pc}^{-2}$ (Section 5.1). For $\alpha_{\rm CO\,(1-0)}$ case, one can simply replace the power-law index with −0.22.

One of the future directions we will take is to study how $\alpha_{\rm CO}$ correlates with physical quantities at cloud scales instead of kpc scales and build $\alpha_{\rm CO}$ prescriptions accordingly. The advantage in this direction is that the physical quantities at the cloud scale are more strongly linked to the fundamental physics of CO emission and dynamics of molecular clouds. For instance, based on the $\alpha_{\rm CO}$ measurements in this work, Teng et al. (2024) have reported an $\alpha_{\rm CO}$ dependence with the cloud-scale velocity dispersion, which likely traces CO opacity change. We also refer the readers to Teng et al. (2022, 2023) for more details.

The other possible future direction for dust-based $\alpha_{\rm CO}$ is a new strategy that simultaneously allows for variations in $\alpha_{\rm CO}$, the dust properties (e.g., D/M in Appendix and dust opacity in Section 3.1), and metallicity at the best-possible resolution. The Leroy et al. (2011) and (Sandstrom et al. 2013, their Appendix A) strategy is a good demonstration of the concept for most items on the list except the resolution. A more sophisticated strategy would help identify the next step forward on $\alpha_{\rm CO}$ prescriptions. We are also interested in investigating whether the $\Sigma_\star$-dependence still applies to $\Sigma_{\rm gas}$-dominated environments.

6.2. Interpreting the Environmental Dependence of α CO

In this section, we will discuss the physical interpretations of the correlations between $\alpha_{\rm CO}$ and the physical quantities we present in the previous sections. As we mentioned in Section 1, we expect two main trends in the variation in $\alpha_{\rm CO}$: (1) the "CO-dark gas" trend, where $\alpha_{\rm CO}$ increases toward lower metallicity as shielding for CO weakens; (2) the "starburst conversion factor" trend, where $\alpha_{\rm CO}$ decreases toward galaxy centers and (U)LIRGs with the decrease in CO optical depth or increase in CO excitation.

Regarding the CO-dark gas trend, we observe moderate to weak anticorrelation between $\alpha_{\rm CO}$ and 12 + log(O/H) at the kpc scale (Section 4.1) and moderate anticorrelation at the galaxy scale (Section 4.2). One possible explanation for the weak correlation is that the statistical significance becomes weaker with the small dynamic range of our 12 + log(O/H) data: 80% of the 12 + log(O/H) measurements fall within a 0.2 dex range from 8.4 to 8.6. The $\alpha_{\rm CO}$-$\Sigma_\star$ relation we present in Section 5 is unlikely caused by this CO-dark gas effect as the dynamic range in 12 + log(O/H) is even smaller for data above the $\Sigma_{\star,\rm T}$ threshold. Another explanation is that the CO-dark gas effect is weaker at nearly solar metallicity (e.g., Wolfire et al. 2010; Glover & Mac Low 2011; Hunt et al. 2015). However, we note that recent simulations show that there is a significant fraction of CO-dark gas ($f_{\rm dark}$) up to the solar metallicity; e.g., Gong et al. (2018) found that $f_{\rm dark}$ ranges

[25] Considering the product of log x and the uncertainties in m.

from 26%–79%. These studies found that $f_{\rm dark}$ correlates with extinction and/or $W_{\rm CO}$ (Smith et al. 2014; Gong et al. 2018, 2020; Hu et al. 2022).

We interpret $\overline{U}$ and (r)sSFR as empirical tracers for regions with high SFR, where the "starburst conversion factor" trend matters and lowers down $\alpha_{\rm CO}$. Some studies have also argued that $\alpha_{\rm CO}$ could decrease with increased radiation field due to CO dissociation (Israel 1997b; Wolfire et al. 2010; Accurso et al. 2017). However, we did not observe this trend, and one possible explanation is that the CO dissociation effect should be weak as long as the CO emission is optically thick (Wolfire et al. 2010; Bolatto et al. 2013). $\Sigma_{\rm SFR}$, which simultaneously traces the UV radiation and starburst regions, also has moderate anticorrelation with $\alpha_{\rm CO}$ across all cases. In general, we observe a stronger correlation between $\Sigma_{\rm SFR}$ and $\alpha_{\rm CO\,(2-1)}$ than $\alpha_{\rm CO\,(1-0)}$. We also observe moderate anticorrelation between $W_{\rm CO}$ and $\alpha_{\rm CO}$. This is consistent with the theoretical assumption under optically thick assumption Bolatto et al. (2013) and recent observations (Hunt et al. 2023).

We interpret the $\alpha_{\rm CO}$-to-$\Sigma_\star$ anticorrelation as the increase in the velocity dispersion of molecular gas from additional gravity. Bolatto et al. (2013; also see Hirashita 2023) suggested that in high-$\Sigma_\star$ environments, the molecular gas experiences gravitational potential from stellar sources, ending up with a total pressure larger than isolated, virialized clouds. This larger pressure results in a gas line width larger than one would expect from self-gravitating clouds. This increase in gas line width scales with total mass (stars and gas) in the system, or $\alpha_{\rm CO} \propto (M_{\rm mol}/(M_{\rm mol} + M_\star))^{0.5}$. The above functional form approximates an $\alpha_{\rm CO}$-to-$\Sigma_\star$ power law in $M_\star$-dominated regions. For the argument to hold, the CO emission must be optically thick. Bolatto et al. (2013) mentioned that the only possible structure for molecular gas that satisfies this scenario is an extended molecular medium.

6.3. Comparing to Previous αCO Surveys

In this section, we compare our measurements to $\alpha_{\rm CO}$ values obtained in previous dust-based $\alpha_{\rm CO}$ surveys. As we will cover studies with both $\alpha_{\rm CO\,(2-1)}$ and $\alpha_{\rm CO\,(1-0)}$ measurements, we will convert $\alpha_{\rm CO\,(2-1)}$ values in literature and this work to $\alpha_{\rm CO\,(1-0)}$ with $R_{21} = 0.65$ for simplicity and uniformity. First, we compare our $\alpha_{\rm CO}$ maps with Sandstrom et al. (2013). They measured spatially resolved $\alpha_{\rm CO}$ in 26 nearby, star-forming galaxies using a dust-based methodology (also see Leroy et al. 2011; den Brok et al. 2023; Yasuda et al. 2023). They assume that the variation in D/G is minimal in a few-kpc-scale "solution pixel" consisting of 37 samples in a hexagonal region and fit D/G and $\alpha_{\rm CO}$ simultaneously from data by minimizing the variation in D/G. Sandstrom et al. (2013) used CO (2–1) data from HERACLES (Leroy et al. 2009b) and $R_{21} = 0.7$. We rescale their results with $R_{21} = 0.65$ for uniformity. Compared to our work, the Sandstrom et al. (2013) methology has larger degrees of freedom for the spatial variation in D/G and D/M. Meanwhile, it is more difficult to push their methodology to a larger sample size at a fixed physical resolution.

There are 13 galaxies that are studied in both (Sandstrom et al. 2013, see their Figure 7) and this work. We show the $\alpha_{\rm CO}$ measurements from both works as a function of the galactocentric radius ($R_{\rm g}$ in terms of R_{25}) in Figure 12. We adopt R_{25} values in this work instead of the Sandstrom et al. (2013) values. The simple mean $\alpha_{\rm CO}$ of all measurements in Sandstrom et al. (2013) is $\sim 2.3\ M_\odot\ {\rm pc}^{-2} ({\rm K\ km\ s}^{-1})^{-1}$. Similar to Sandstrom et al. (2013), we find a weak to moderate (but significant) positive correlation between $\alpha_{\rm CO}$ and $R_{\rm g}$. When we normalize the $\alpha_{\rm CO}$ in each galaxy by the mean $\alpha_{\rm CO}$ in each galaxy ($<\alpha_{\rm CO,gal}>$), both works show a flat trend with the radius in the mid-to-outer disk. The Sandstrom et al. (2013) data show a more significant decrease in $\alpha_{\rm CO}$ in the galaxy center. Several factors could contribute to the difference in the innermost radial bins. If we calculate the $W_{\rm CO}$-weighted mean instead of the median in each bin, the difference in the bin with the smallest radii will decrease by 0.1 dex, which partially explains the discrepancy. Another possible explanation is that some of the measurements with small $\Sigma_{\rm mol}$ (and possibly small $\alpha_{\rm CO}$) are removed due to small S/N; however, they are taken into account in Sandstrom et al. (2013). It is not clear whether the difference in resolution is a cause. When we calculate $\alpha_{\rm CO}$ at 1 kpc resolution with the galaxies with distance within 10 Mpc, there is no clear trend of the resulting $\alpha_{\rm CO}$ with resolution. The fixed D/M is unlikely to be a major cause as the Sandstrom et al. (2013) results are consistent with a D/G-metallicity power law (see their Figure 13).

For comparing galaxy-averaged $\alpha_{\rm CO}$ measurements, we include another previous study: the COMING survey (Sorai et al. 2019; Yasuda et al. 2023). The COMING survey solves D/G and $\alpha_{\rm CO\,(1-0)}$ simultaneously by minimizing a χ^2 value defined by the difference between (D/G $\times$ ($\Sigma_{\rm atom} + \alpha_{\rm CO\,(1-0)} W_{\rm CO\,(1-0)}$)) and $\Sigma_{\rm dust}$ derived from dust SED fitting. Here, we quote their "global" result, where the authors fit all data within one galaxy to retrieve one set of D/G and $\alpha_{\rm CO}$ values.

We compare our measured $\alpha_{\rm CO}$ in each galaxy with Sandstrom et al. (2013) and the COMING survey (Sorai et al. 2019; Yasuda et al. 2023) in Figure 13. For Sandstrom et al. (2013) and this work, we adopt the $W_{\rm CO}$-weighted mean. For the COMING survey, we adopt their "global" result. The $\alpha_{\rm CO}$ measured in the three works are, in general, consistent with each other within uncertainties. Our measurements made with CO (2–1) and CO (1–0) agree with each other. When there is a difference, it is more often that the one derived with CO (2–1) has a slightly larger value. We also note that in several galaxies with signatures of active galactic nuclei (AGN; see classification in Kennicutt et al. 2011), there is a larger offset between our measurements and literature, e.g., NGC3627 and NGC4725; however, there are also galaxies with AGN show consistent results, e.g., NGC4536, NGC4736, and NGC5055. Thus, having AGN is not the only cause for the mismatch, and it is likely that the type of nuclei activities do not dominate the kpc-scale $\alpha_{\rm CO}$ values (e.g., Sandstrom et al. 2013). The adopted dust SED fitting method is also unlikely the cause for the difference in NGC4725 as we have a lower estimate of $\Sigma_{\rm dust}$, which should yield smaller $\alpha_{\rm CO}$. Our measurements made with CO (1–0) generally agree with the COMING survey.

7. Summary

In this work, we measure the spatially resolved CO-to-H_2 conversion factor ($\alpha_{\rm CO}$) in 37 nearby galaxies at 2 kpc resolution. We derive $\Sigma_{\rm mol}$ by using a fixed D/M and converting $\Sigma_{\rm dust}$ and Z into $\Sigma_{\rm gas}$, then removing $\Sigma_{\rm atom}$ to get $\Sigma_{\rm mol}$. We calculate $\alpha_{\rm CO}$ with derived $\Sigma_{\rm mol}$ and measured $W_{\rm CO}$. In total, we have $\sim$810 and $\sim$610 independent measurements of $\alpha_{\rm CO}$ for CO (2–1) and CO (1–0) data, respectively. The mean values for $\alpha_{\rm CO\,(2-1)}$ and $\alpha_{\rm CO\,(1-0)}$ are $9.7^{+4.7}_{-5.7}$ and $4.2^{+1.9}_{-2.0}\ M_\odot\ {\rm pc}^{-2} ({\rm K\ km\ s}^{-1})^{-1}$, respectively. The CO-intensity-weighted mean for $\alpha_{\rm CO\,(2-1)}$ is $5.76\,M_\odot$ pc^{-2}(K km s^{-1})$^{-1}$, and $3.33\,M_\odot$ pc^{-2}(K km s^{-1})$^{-1}$ for $\alpha_{\rm CO\,(1-0)}$. These values are measured in 37 galaxies with data S/N > 1.

We examine how $\alpha_{\rm CO}$ scales with several physical quantities, i.e., $W_{\rm CO}$, metallicity, $\Sigma_{\rm dust}$, ISRF, $\Sigma_\star$, $\Sigma_{\rm SFR}$, and (r)sSFR. At 2 kpc scale, all quantities have significant local correlation with $\alpha_{\rm CO}$. Among them, the strength of the ISRF ($\overline{U}$), $\Sigma_{\rm SFR}$, and $W_{\rm CO}$ have the strongest anticorrelation with spatially resolved $\alpha_{\rm CO}$. We provide linear regression of $\alpha_{\rm CO}$ with all the quantities tested, along with the corresponding performance and uncertainties in Table 3.

At the galaxy-integrated scale, most quantities have a significant correlation with $W_{\rm CO}$-weighted mean $\alpha_{\rm CO}$. $\overline{U}$, $\Sigma_{\rm SFR}$, $W_{\rm CO}$ and 12 + log(O/H) have significant correlations with $\alpha_{\rm CO}$ for both CO (1–0) and CO (2–1) cases.

When we normalized resolved $\alpha_{\rm CO}$ measurements by the $W_{\rm CO}$-weighted mean in each galaxy, we found an increased correlation strength between normalized $\alpha_{\rm CO}$ and $\Sigma_\star$. After examining through $\Sigma_\star$ bins, we find that in regions with high stellar mass surface densities ($\Sigma_\star \geqslant 100\,M_\odot{\rm pc}^{-2}$), the $\alpha_{\rm CO}$ decreases with $\Sigma_\star$. In particular, we find:

$$\begin{cases} \alpha_{\rm CO\,(2-1)}/\alpha_{\rm CO\,(2-1),T} \propto \Sigma_\star^{-0.48} \\ \alpha_{\rm CO\,(1-0)}/\alpha_{\rm CO\,(1-0),T} \propto \Sigma_\star^{-0.22} \end{cases}, \quad \Sigma_\star \geqslant \Sigma_{\star,{\rm T}}, \tag{21}$$

within D/M = 0.4–0.7; the D/M values for the inner disk are inferred from literature. The power-law index is insensitive to the assumed D/M, and it is roughly constant in the range of $60 \leqslant \Sigma_{\star,{\rm T}} \leqslant 300\,M_\odot{\rm pc}^{-2}$. It also has little dependence on the adopted ratio between CO rotational lines.

When fitting the power-law relation within individual galaxies, we find significant dependence of the normalization of $\alpha_{\rm CO}$ in each galaxy on several quantities. Among them, the linear regression to $\log \overline{U}_{\rm gal}$ has minimal statistical uncertainties. Thus, we recommend using $\Sigma_\star$ and $\log \overline{U}_{\rm gal}$ to predict $\alpha_{\rm CO}$ at high-$\Sigma_\star$ environments.

This decrease in $\alpha_{\rm CO}$ in the high-$\Sigma_\star$ region is likely due to the increased CO brightness with increased line width. The line width is larger than self-gravitating clouds due to the additional gravity from stellar sources, and the structure satisfying this scenario is likely an extended molecular medium. Understanding the decrease in $\alpha_{\rm CO}$ at high $\Sigma_\star$ is important for accurately assessing molecular gas content and star formation efficiency in the centers of galaxies and bridges the "MW-like" to "starburst" conversion factor.

Acknowledgments

We thank the anonymous referee for the detailed and constructive comments that helped to improve this work. I.C. thanks Hiroyuki Hirashita for helpful discussions. I.C. thanks the National Science and Technology Council for support through grant 111-2112-M-001-038-MY3, and the Academia Sinica for Investigator Award AS-IA-109-M02 (PI: Hiroyuki Hirashita). K.S. and Y.T. acknowledge funding support from NRAO Student Observing Support grant SOSPADA-012 and from the National Science Foundation (NSF) under grant No. 2108081. J.S. acknowledges support by NASA through the NASA Hubble Fellowship grant HST-HF2-51544 awarded by the Space Telescope Science Institute (STScI), which is operated by the Association of Universities for Research in Astronomy, Inc., for NASA, under contract NAS5-26555. A.D. B. acknowledges support from the National Science Foundation through grants AST-2108140 and AST-2307441. E.W.K. acknowledges support from the Smithsonian Institution as a Submillimeter Array (SMA) Fellow and the Natural Sciences and Engineering Research Council of Canada. J.C. acknowledges support from ERC starting grant #851622 DustOrigin.

This work uses observations made with the ESA Herschel Space Observatory. Herschel is an ESA space observatory with science instruments provided by European-led Principal Investigator consortia and with important participation from NASA. The Herschel spacecraft was designed, built, tested, and launched under a contract to ESA managed by the Herschel/Planck Project team by an industrial consortium under the overall responsibility of the prime contractor Thales Alenia Space (Cannes), and including Astrium (Friedrichshafen) responsible for the payload module and for system testing at spacecraft level, Thales Alenia Space (Turin) responsible for the service module, and Astrium (Toulouse) responsible for the telescope, with in excess of a hundred subcontractors.

This paper makes use of VLA data with project codes 14A-468, 14B-396, 16A-275, and 17A-073, which have been processed as part of the EveryTHINGS survey. This paper makes use of the VLA data with legacy ID AU157, which has been processed in the PHANGS-VLA survey. The National Radio Astronomy Observatory is a facility of the National Science Foundation operated under a cooperative agreement by Associated Universities, Inc. This publication makes use of data products from the Wide-field Infrared Survey Explorer, which is a joint project of the University of California, Los Angeles, and the Jet Propulsion Laboratory/California Institute of Technology, funded by the National Aeronautics and Space Administration.

This paper makes use of the following ALMA data, which have been processed as part of the PHANGS-ALMA CO(2–1) survey: ADS/JAO.ALMA#2012.1.00650.S, ADS/JAO.ALMA#2015.1.00782.S, ADS/JAO.ALMA#2018.1.01321.S, ADS/JAO.ALMA#2018.1.01651.S. ALMA is a partnership of ESO (representing its member states), NSF (USA), and NINS (Japan), together with NRC (Canada), MOST and ASIAA (Taiwan), and KASI (Republic of Korea), in cooperation with the Republic of Chile. The Joint ALMA Observatory is operated by ESO, AUI/NRAO, and NAOJ.

This research made use of Astropy,[26] a community-developed core Python package for Astronomy (Astropy Collaboration et al. 2013, 2018, 2022). This research has made use of NASA's Astrophysics Data System Bibliographic Services. We acknowledge the usage of the HyperLeda database (http://leda.univ-lyon1.fr). This research has made use of the NASA/IPAC Extragalactic Database (NED), which is funded by the National Aeronautics and Space Administration and operated by the California Institute of Technology.

Facility: ALMA, Herschel, IRAM:30 m, VLA, WISE, WSRT

Software: astropy (Astropy Collaboration et al. 2013, 2018, 2022), matplotlib (Hunter 2007), numpy & scipy (van der Walt et al. 2011)

[26] http://www.astropy.org

Appendix
Internal Variation in D/M

It is questionable whether D/M is a constant within galaxies, even in galaxy centers. Observations have found internal variations of D/M within galaxies (Jenkins 2009; Roman-Duval et al. 2014, 2017; Chiang et al. 2018; Vílchez et al. 2019). In these studies, people found a higher D/M toward higher metallicity or gas surface densities. A varying D/M within galaxies is also expected by several models (Hou et al. 2019; Li et al. 2019; Aoyama et al. 2020). However, how to characterize the variation in D/M with local conditions is a topic that remains unsolved, and it is outside the main scope of this work.

To demonstrate how a varying D/M might affect our results, we define a toy model with D/M increasing toward galaxy centers. For the galaxy disks ($R_g > R_e$), we assume D/M = 0.4. This value is inspired by several recent studies, e.g., ∼0.5 in Draine et al. (2014), 0.5 ± 0.1 in Clark et al. (2016), 0.4 ± 0.2 in Clark et al. (2019), and $0.46^{+0.12}_{-0.06}$ in Chiang et al. (2021). For the very center of the galaxies ($R_g = 0$), we assume an efficient dust growth, i.e., all refractory elements are completely depleted and gaseous elements (e.g., oxygen and nitrogen) are partially depleted, and adopted D/M = 0.7 from Feldmann (2015). In $R_e \geqslant R_g \geqslant 0$, we assume a smooth transition, that is:

$$\mathrm{D/M} = \begin{cases} 0.7 - 0.3 \times R_g/R_e, & R_g \leqslant R_e \\ 0.4, & R_g > R_e \end{cases}. \tag{A1}$$

With this toy model, we find $a = -0.74^{+0.06}_{-0.08}$ and $-0.47^{+0.04}_{-0.05}$ for CO (2–1) and CO (1–0), respectively. These indices are steeper than our fiducial case, i.e., constant D/M, indicating that the α_{CO}-to-$\Sigma_\star$ relation observed in Section 5 is not caused by the variation in dust properties. Although we do expect an internal variation in D/M, the variation in the galaxy center predicted in simulations is more gentle than our toy model (Choban et al. 2022; Romano et al. 2022). Thus the calculation with this toy model should be interpreted as an extreme case. The constant D/M case and the toy model case should sandwich the actual indices.

ORCID iDs

I-Da Chiang (江宜達) https://orcid.org/0000-0003-2551-7148
Karin M. Sandstrom https://orcid.org/0000-0002-4378-8534
Jérémy Chastenet https://orcid.org/0000-0002-5235-5589
Alberto D. Bolatto https://orcid.org/0000-0002-5480-5686
Eric W. Koch https://orcid.org/0000-0001-9605-780X
Adam K. Leroy https://orcid.org/0000-0002-2545-1700
Jiayi Sun (孙嘉懿) https://orcid.org/0000-0003-0378-4667
Yu-Hsuan Teng https://orcid.org/0000-0003-4209-1599
Thomas G. Williams https://orcid.org/0000-0002-0012-2142

References

Abdo, A. A., Ackermann, M., Ajello, M., et al. 2010, ApJ, 710, 133
Accurso, G., Saintonge, A., Catinella, B., et al. 2017, MNRAS, 470, 4750
Ackermann, M., Ajello, M., Allafort, A., et al. 2012, ApJ, 755, 22
Aniano, G., Draine, B. T., Gordon, K. D., & Sandstrom, K. 2011, PASP, 123, 1218
Aoyama, S., Hirashita, H., & Nagamine, K. 2020, MNRAS, 491, 3844
Asano, R. S., Takeuchi, T. T., Hirashita, H., & Inoue, A. K. 2013, EP&S, 65, 213
Asplund, M., Grevesse, N., Sauval, A. J., & Scott, P. 2009, ARA&A, 47, 481
Astropy Collaboration, Price-Whelan, A. M., Lim, P. L., et al. 2022, ApJ, 935, 167
Astropy Collaboration, Price-Whelan, A. M., Sipőcz, B. M., et al. 2018, AJ, 156, 123
Astropy Collaboration, Robitaille, T. P., Tollerud, E. J., et al. 2013, A&A, 558, A33
Belfiore, F., Leroy, A. K., Sun, J., et al. 2023, A&A, 670, A67
Berg, D. A., Pogge, R. W., Skillman, E. D., et al. 2020, ApJ, 893, 96
Bolatto, A. D., Leroy, A. K., Jameson, K., et al. 2011, ApJ, 741, 12
Bolatto, A. D., Wolfire, M., & Leroy, A. K. 2013, ARA&A, 51, 207
Carleton, T., Cooper, M. C., Bolatto, A. D., et al. 2017, MNRAS, 467, 4886
Chastenet, J., Sandstrom, K., Chiang, I.-D., et al. 2021, ApJ, 912, 103
Chiang, I.-D., Hirashita, H., Chastenet, J., et al. 2023, MNRAS, 520, 5506
Chiang, I.-D., Sandstrom, K. M., Chastenet, J., et al. 2018, ApJ, 865, 117
Chiang, I.-D., Sandstrom, K. M., Chastenet, J., et al. 2021, ApJ, 907, 29
Choban, C. R., Keres, D., Hopkins, P. F., et al. 2022, MNRAS, 514, 4506
Clark, C. J. R., De Vis, P., Baes, M., et al. 2019, MNRAS, 489, 5256
Clark, C. J. R., Schofield, S. P., Gomez, H. L., & Davies, J. I. 2016, MNRAS, 459, 1646
Cormier, D., Bigiel, F., Jiménez-Donaire, M. J., et al. 2018, MNRAS, 475, 3909
Croxall, K. V., Pogge, R. W., Berg, D. A., Skillman, E. D., & Moustakas, J. 2016, ApJ, 830, 4
De Blok, W. J. G., Walter, F., Brinks, E., et al. 2008, AJ, 136, 2648
De Vis, P., Jones, A., Viaene, S., et al. 2019, A&A, 623, A5
den Brok, J. S., Bigiel, F., Chastenet, J., et al. 2023, A&A, 676, A93
den Brok, J. S., Chatzigiannakis, D., Bigiel, F., et al. 2021, MNRAS, 504, 3221
Downes, D., & Solomon, P. M. 1998, ApJ, 507, 615
Downes, D., Solomon, P. M., & Radford, S. J. E. 1993, ApJL, 414, L13
Draine, B. T., Aniano, G., Krause, O., et al. 2014, ApJ, 780, 172
Draine, B. T., & Hensley, B. S. 2021, ApJ, 909, 94
Draine, B. T., & Li, A. 2007, ApJ, 657, 810
Druard, C., Braine, J., Schuster, K. F., et al. 2014, A&A, 567, A118
Dunne, L., Maddox, S. J., Papadopoulos, P. P., Ivison, R. J., & Gomez, H. L. 2022, MNRAS, 517, 962
Dwek, E. 1998, ApJ, 501, 643
Emsellem, E., Schinnerer, E., Santoro, F., et al. 2022, A&A, 659, A191
Esteban, C., Méndez-Delgado, J. E., García-Rojas, J., & Arellano-Córdova, K. Z. 2022, ApJ, 931, 92
Feldmann, R. 2015, MNRAS, 449, 3274
Galliano, F., Galametz, M., & Jones, A. P. 2018, ARA&A, 56, 673
Genzel, R., Tacconi, L. J., Combes, F., et al. 2012, ApJ, 746, 69
Glover, S. C. O., & Mac Low, M. M. 2011, MNRAS, 412, 337
Gong, M., Ostriker, E. C., Kim, C.-G., & Kim, J.-G. 2020, ApJ, 903, 142
Gong, M., Ostriker, E. C., & Kim, C.-G. 2018, ApJ, 858, 16
Gratier, P., Braine, J., Rodriguez-Fernandez, N. J., et al. 2010, A&A, 522, A3
Grenier, I. A., Casandjian, J.-M., & Terrier, R. 2005, Sci, 307, 1292
Groves, B., Kreckel, K., Santoro, F., et al. 2023, MNRAS, 520, 4902
Heald, G., Józsa, G., Serra, P., et al. 2011, A&A, 526, A118
Herrero-Illana, R., Privon, G. C., Evans, A. S., et al. 2019, A&A, 628, A71
Hirashita, H. 2023, MNRAS, 522, 4612
Hirashita, H., & Chiang, I. D. 2022, MNRAS, 516, 1612
Hirashita, H., & Kuo, T.-M. 2011, MNRAS, 416, 1340
Hirashita, H., & Voshchinnikov, N. V. 2014, MNRAS, 437, 1636
Hou, K.-C., Aoyama, S., Hirashita, H., Nagamine, K., & Shimizu, I. 2019, MNRAS, 485, 1727
Hu, C.-Y., Schruba, A., Sternberg, A., & van Dishoeck, E. F. 2022, ApJ, 931, 28
Hunt, L. K., Belfiore, F., Lelli, F., et al. 2023, A&A, 675, A64
Hunt, L. K., García-Burillo, S., Casasola, V., et al. 2015, A&A, 583, A114
Hunter, J. D. 2007, CSE, 9, 90
Israel, F. P. 1997a, A&A, 317, 65
Israel, F. P. 1997b, A&A, 328, 471
Israel, F. P. 2009a, A&A, 493, 525
Israel, F. P. 2009b, A&A, 506, 689
Israel, F. P. 2020, A&A, 635, A131
Issa, M. R., MacLaren, I., & Wolfendale, A. W. 1990, A&A, 236, 237
Jenkins, E. B. 2009, ApJ, 700, 1299
Jenkins, E. B., & Wallerstein, G. 2017, ApJ, 838, 85
Kennicutt, R. C., Calzetti, D., Aniano, G., et al. 2011, PASP, 123, 1347
Koch, E. W., Rosolowsky, E. W., Lockman, F. J., et al. 2018, MNRAS, 479, 2505
Kreckel, K., Ho, I. T., Blanc, G. A., et al. 2019, ApJ, 887, 80

Kuno, N., Sato, N., Nakanishi, H., et al. 2007, PASJ, 59, 117
Lang, P., Meidt, S. E., Rosolowsky, E., et al. 2020, ApJ, 897, 122
Leroy, A., Bolatto, A., Stanimirovic, S., et al. 2007, ApJ, 658, 1027
Leroy, A. K., Bolatto, A., Bot, C., et al. 2009a, ApJ, 702, 352
Leroy, A. K., Bolatto, A., Gordon, K., et al. 2011, ApJ, 737, 12
Leroy, A. K., Bolatto, A. D., Sandstrom, K., et al. 2023, ApJL, 944, L10
Leroy, A. K., Rosolowsky, E., Usero, A., et al. 2022, ApJ, 927, 149
Leroy, A. K., Sandstrom, K. M., Lang, D., et al. 2019, ApJS, 244, 24
Leroy, A. K., Schinnerer, E., Hughes, A., et al. 2021, ApJS, 257, 43
Leroy, A. K., Walter, F., Bigiel, F., et al. 2009b, AJ, 137, 4670
Li, Q., Narayanan, D., & Davé, R. 2019, MNRAS, 490, 1425
Madden, S. C., Cormier, D., Hony, S., et al. 2020, A&A, 643, A141
Makarov, D., Prugniel, P., Terekhova, N., Courtois, H., & Vauglin, I. 2014, A&A, 570, A13
Martin, D. C., Fanson, J., Schiminovich, D., et al. 2005, ApJL, 619, L1
McCormick, A., Veilleux, S., & Rupke, D. S. N. 2013, ApJ, 774, 126
McKee, C. F., & Ostriker, E. C. 2007, ARA&A, 45, 565
Meidt, S. E., Rand, R. J., & Merrifield, M. R. 2009, ApJ, 702, 277
Muñoz-Mateos, J. C., Gil de Paz, A., Zamorano, J., et al. 2009, ApJ, 703, 1569
Narayanan, D., Krumholz, M. R., Ostriker, E. C., & Hernquist, L. 2012, MNRAS, 421, 3127
Ostriker, E. C., & Shetty, R. 2011, ApJ, 731, 41
Papadopoulos, P. P., Thi, W. F., & Viti, S. 2002, ApJ, 579, 270
Papadopoulos, P. P., van der Werf, P. P., Xilouris, E. M., et al. 2012, MNRAS, 426, 2601
Péroux, C., & Howk, J. C. 2020, ARA&A, 58, 363
Pilbratt, G. L., Riedinger, J. R., Passvogel, T., et al. 2010, A&A, 518, L1
Pilyugin, L. S., & Grebel, E. K. 2016, MNRAS, 457, 3678
Planck Collaboration, Ade, P. A. R., Aghanim, N., et al. 2011, A&A, 536, A19
Puche, D., Carignan, C., & Bosma, A. 1990, AJ, 100, 1468
Puche, D., Carignan, C., & van Gorkom, J. H. 1991, AJ, 101, 456
Rémy-Ruyer, A., Madden, S. C., Galliano, F., et al. 2014, A&A, 563, A31
Roman-Duval, J., Bot, C., Chastenet, J., & Gordon, K. 2017, ApJ, 841, 72
Roman-Duval, J., Gordon, K. D., Meixner, M., et al. 2014, ApJ, 797, 86
Roman-Duval, J., Jenkins, E. B., Tchernyshyov, K., et al. 2022, ApJ, 928, 90
Roman-Duval, J., Jenkins, E. B., Williams, B., et al. 2019, ApJ, 871, 151
Romano, L. E. C., Nagamine, K., & Hirashita, H. 2022, MNRAS, 514, 1441
Sánchez, S. F., Barrera-Ballesteros, J. K., López-Cobá, C., et al. 2019, MNRAS, 484, 3042
Sánchez, S. F., Rosales-Ortega, F. F., Iglesias-Páramo, J., et al. 2014, A&A, 563, A49
Sandstrom, K. M., Leroy, A. K., Walter, F., et al. 2013, ApJ, 777, 5
Santoro, F., Kreckel, K., Belfiore, F., et al. 2022, A&A, 658, A188
Schruba, A., Leroy, A. K., Kruijssen, J. M. D., et al. 2017, ApJ, 835, 278
Schruba, A., Leroy, A. K., Walter, F., et al. 2011, AJ, 142, 37
Schruba, A., Leroy, A. K., Walter, F., et al. 2012, AJ, 143, 138
Shetty, R., Glover, S. C., Dullemond, C. P., et al. 2011, MNRAS, 415, 3253
Shetty, R., Kauffmann, J., Schnee, S., & Goodman, A. A. 2009a, ApJ, 696, 676
Shetty, R., Kauffmann, J., Schnee, S., Goodman, A. A., & Ercolano, B. 2009b, ApJ, 696, 2234
Smith, R. J., Glover, S. C. O., Clark, P. C., Klessen, R. S., & Springel, V. 2014, MNRAS, 441, 1628
Sofue, Y., Tutui, Y., Honma, M., et al. 1999, ApJ, 523, 136
Solomon, P. M., Rivolo, A. R., Barrett, J., & Yahil, A. 1987, ApJ, 319, 730
Sorai, K., Kuno, N., Muraoka, K., et al. 2019, PASJ, 71, S14
Stepnik, B., Abergel, A., Bernard, J. P., et al. 2003, A&A, 398, 551
Strong, A. W., & Mattox, J. R. 1996, A&A, 308, L21
Sun, J., Leroy, A. K., Ostriker, E. C., et al. 2020, ApJ, 892, 148
Sun, J., Leroy, A. K., Schruba, A., et al. 2018, ApJ, 860, 172
Swaters, R. A., van Albada, T. S., van der Hulst, J. M., & Sancisi, R. 2002, A&A, 390, 829
Teng, Y.-H., Chiang, I. D., Sandstrom, K. M., et al. 2024, ApJ, 961, 42
Teng, Y.-H., Sandstrom, K. M., Sun, J., et al. 2022, ApJ, 925, 72
Teng, Y.-H., Sandstrom, K. M., Sun, J., et al. 2023, ApJ, 950, 119
Tully, R. B., Rizzi, L., Shaya, E. J., et al. 2009, AJ, 138, 323
van der Walt, S., Colbert, S. C., & Varoquaux, G. 2011, CSE, 13, 22
Vílchez, J. M., Relaño, M., Kennicutt, R., et al. 2019, MNRAS, 483, 4968
Walter, F., Brinks, E., de Blok, W. J. G., et al. 2008, AJ, 136, 2563
Williams, T. G., Kreckel, K., Belfiore, F., et al. 2022, MNRAS, 509, 1303
Wolfire, M. G., Hollenbach, D., & McKee, C. F. 2010, ApJ, 716, 1191
Wright, E. L., Eisenhardt, P. R. M., Mainzer, A. K., et al. 2010, AJ, 140, 1868
Yajima, Y., Sorai, K., Miyamoto, Y., et al. 2021, PASJ, 73, 257
Yasuda, A., Kuno, N., Sorai, K., et al. 2023, PASJ, 75, 743
Zurita, A., Florido, E., Bresolin, F., Pérez-Montero, E., & Pérez, I. 2021, MNRAS, 500, 2359